



# Lateral variations in the Unit 7–8 boundary zone of the Rum Eastern Layered Intrusion, NW Scotland: implications for the origin and timing of Cr-spinel seam formation

Felix E. D. Kaufmann<sup>1,2</sup> · Brian O'Driscoll<sup>3</sup> · Lutz Hecht<sup>1,2</sup>

Received: 27 December 2019 / Accepted: 13 August 2020 / Published online: 2 September 2020  
© The Author(s) 2020

## Abstract

The Rum Layered Suite, NW Scotland, hosts Cr-spinel seams at the bases of peridotite–troctolite macro-rhythmic units in the eastern portion of the intrusion. Here, we present detailed field observations together with microstructural and mineral chemical analyses for the Unit 7–8 Cr-spinel seam and associated cumulates in the Eastern Layered Intrusion. Detailed mapping and sampling reveal significant lateral variations in the structural characteristics and mineral compositions of the Unit 7–8 boundary zone rocks. Although the Cr-spinel seam is laterally continuous over ~3 km, it is absent towards the centre and the margins of the intrusion. The compositional characteristics of Cr-spinel and plagioclase vary systematically along strike, exhibiting a chemical evolution towards more differentiated compositions with increasing distance from the main feeder conduit of the Rum intrusion; the Long Loch Fault. On the basis of our combined datasets, we propose that the upper part of the troctolite, the anorthosite layer underlying the Cr-spinel seam and the seam itself formed during a multi-stage magma replenishment event. The stages can be summarised as follows: (1) peridotite schlieren and anorthosite autoliths formed following melt infiltration and cumulate assimilation in the crystal mush of the Unit 7 troctolite. (2) The anorthosite layer then formed from the Unit 7 troctolite crystal mush by thermal erosion and dissolution due to infiltrating magma. (3) Subsequent dissolution of the anorthosite layer by new replenishing magma led to peritectic in situ crystallisation of the Unit 7–8 Cr-spinel seam, with (4) continued magma input eventually producing the overlying Unit 8 peridotite. In the central part of the Rum Layered Suite, the aforementioned assimilation of the troctolitic footwall formed the anorthosite layer. However, the absence of anorthosite in close proximity to the Long Loch Fault can be explained by enhanced thermochemical erosion close to the feeder zone, and its absence close to the margins of the intrusion, at maximum distance from the Long Loch Fault, may be due to cooling of the magma and loss of erosion potential. In line with other recent studies on PGE-bearing chromitites in layered intrusions, we highlight the importance of multi-stage intrusive magma replenishment to the formation of spatially coupled anorthosite and Cr-spinel seams, as well as the lateral mineral chemical variations observed in the Unit 7–8 boundary zone cumulates.

Communicated by Othmar Müntener.

**Electronic supplementary material** The online version of this article (<https://doi.org/10.1007/s00410-020-01732-x>) contains supplementary material, which is available to authorized users.

✉ Felix E. D. Kaufmann  
felix.kaufmann@mfn-berlin.de

- <sup>1</sup> Leibniz-Institut für Evolutions- Und Biodiversitätsforschung, Museum für Naturkunde Berlin, Invalidenstr. 43, 10115 Berlin, Germany
- <sup>2</sup> Institut für Geologische Wissenschaften, Freie Universität Berlin, Malteserstr. 74–100, 12449 Berlin, Germany
- <sup>3</sup> Department of Earth and Environmental Sciences, University of Manchester, Oxford Road, Manchester M13 9PL, UK

## Introduction

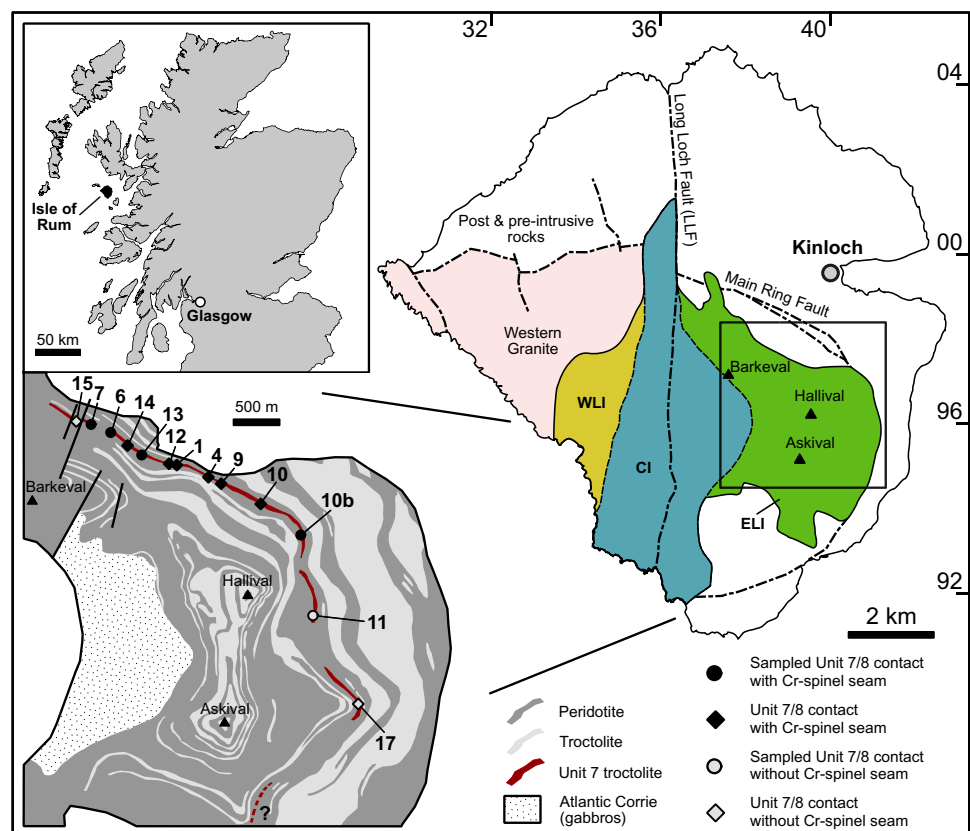
The formation of Cr-spinel seams in layered intrusions remains a controversial phenomenon in igneous petrology (Irvine 1975, 1977; Namur et al. 2015; Wager and Brown 1967). Despite containing some of the world's largest reserves of Cr and associated platinum-group elements (PGE), their petrogenesis is still not well understood, and a variety of contrasting petrological models exist for their formation. These models include magma mixing, changes in pressure or oxygen fugacity or the emplacement of chromite-rich slurries (see Namur et al. 2015 for detailed reviews). The Rum Layered Suite in NW Scotland is a classic example of a layered intrusion that hosts Cr-spinel seams

(Brown 1956; Harker 1908). The Rum Cr-spinel seams have been the objects of careful petrological study for decades (Brown 1956; Emeleus 1994, 1997; Harker 1908; Henderson and Suddaby 1971; Hepworth et al. 2017; O'Driscoll et al. 2009a, 2009b, 2010; Volker and Upton 1990; Young 1984). This is due in part to the fact that some of the seams exhibit significant, albeit sub-economic, enrichment in the PGE (Butcher et al. 1999; O'Driscoll et al. 2009a; Power et al. 2003). In addition, the style of PGE mineralisation in parts of the Rum intrusion is quite similar to that of the economically significant Merensky Reef and UG2 chromitites (Bushveld Complex, South Africa), in that Cr-spinel seams occur at apparently unconformable boundaries in the cumulate section, sandwiched between anorthosite and mafic orthocumulate. Most previous work on the Rum intrusion Cr-spinel seams has focused on discrete vertical sections of the cumulate stratigraphy containing the Cr-spinel seams (O'Driscoll et al. 2009a, 2009b; Power et al. 2000). Unlike other significant PGE reefs (e.g., the Bushveld chromitites noted above), little information exists on the degree to which the Rum Cr-spinel seams exhibit petrographic and/or compositional lateral variations. The most PGE-rich Rum Cr-spinel seams occur at the peridotitic bases of macro-rhythmic layers in the Eastern Layered Intrusion (ELI; Fig. 1), which has been taken by previous workers as evidence that they likely formed during some significant (intrusion-scale)

replenishment of the magma chamber by primitive magma (Dunham and Wadsworth 1978; O'Driscoll et al. 2009a, 2010; Power et al. 2000). Thus, establishing the relationships between the Cr-spinel seams and their host rocks, and whether these vary along strike, could reveal valuable information on the nature and extent of interaction of the replenishing magma with its footwall cumulates leading to precious metal enrichment in the Rum intrusion.

The aim of this study is to advance our understanding of the mechanisms that drive PGE-reef formation in layered intrusions, by characterising the Unit 7–8 Cr-spinel seam and hanging wall-footwall lithologies laterally across the extent of the intrusion. The Unit 7–8 Cr-spinel seam package comprises a diverse assemblage of lithologies (anorthosite, deformed troctolite, multiple Cr-spinel seams) as well as the highest PGE abundances of any of the Rum PGE-reefs (O'Driscoll et al. 2009a). We report detailed field observations and quantify lateral variations in the macro-to-micro-structural and mineral chemical character of the Unit 7–8 Cr-spinel seam and its characteristic host rocks. Our observations reveal that the seam package was constructed by a close interplay of repeated magma replenishment, cumulate assimilation and in situ crystallisation. Notably, we observe a close association of the Cr-spinel seam and the footwall anorthosite layer and propose that assimilation of anorthosite instead of troctolite was needed to induce Cr-spinel seam

**Fig. 1** Location map of the Rum Layered Intrusion, NW Scotland and simplified geological map of the Rum Layered Intrusion, modified after Emeleus (1994). The black box shows the position of the detailed geological map in the lower left corner shows the Unit 7–8 boundary with sample localities. WLI, Western Layered Intrusion; CI Central Intrusion; ELI, Eastern Layered Intrusion



formation. Our explanation may have implications for Cr-spinel seam formation in general, given the frequently observed coupled occurrence of such seams and anorthosite in layered intrusions and ophiolites (e.g. Bédard 1991, 1993; Scoon and Costin 2018). Furthermore, an increasing number of studies have linked Cr-spinel seam formation in layered intrusions to ‘out-of-sequence’ sill-like magma replenishment (Bédard et al. 1988; Mungall et al. 2016; Scoon and Costin 2018; Hepworth et al. 2017; 2018; 2020a, 2020b; Robb and Mungall 2020; Scoon et al. 2020). Thus, we aim to examine the lateral variability of the Unit 7–8 Cr-spinel seam and associated rocks in light of these studies to elucidate whether an intrusive replenishment mechanism for Cr-spinel seam formation might hold here too.

## Geological setting

The Rum Layered Suite (Fig. 1) is a classic example of a mafic–ultramafic layered intrusion (Brown 1956; Wager and Brown 1967). It formed in response to opening of the North Atlantic (Emeleus et al. 1996) at ca. 60 Ma (Hamilton et al. 1998). The intrusion is subdivided into the ELI, Western Layered Intrusion (WLI) and the Central Intrusion (CI). The comparatively well-studied ELI consists of 16 macro-rhythmic units of feldspathic peridotite–troctolite ( $\pm$  olivine gabbro), each of which varies considerably in thickness (Brown 1956; Emelcus et al. 1996). The macro-rhythmic units of the ELI have traditionally been interpreted as representing new batches of replenishing magma (Emeleus et al. 1996; O’Driscoll et al. 2009a) of basaltic-to-picritic composition (Upton et al. 2002). However, an alternate interpretation, originally proposed by Harker (1908) and developed by Bédard et al. (1988), Hepworth et al. (2017) and Hepworth et al. (2020a, 2020b), suggests that the ELI represents an incrementally constructed sill complex. Cr-spinel seams occur at the bases of the 6–7, 7–8, 11–12 and 13–14 units (Brown 1956; O’Driscoll et al. 2009a). These seams are typically 2–5 mm thick and can be traced laterally over much of the 2–3 km extent of the ELI (Emeleus et al. 1996). Elevated PGE concentrations have been reported for the Cr-spinel seams of the ELI (Butcher et al. 1999; O’Driscoll et al. 2009a). O’Driscoll et al. (2009b; 2010) reported that several of the ‘main’ Cr-spinel seams at unit bases are associated with other, thinner, subsidiary seams located several centimetres above and below the unit boundary (e.g., Unit 7–8 and 11–12). Early studies proposed that the Cr-spinel seams formed by crystal settling on top of the solidifying crystal mush (Brown 1956; Dunham and Wilkinson 1985; Henderson and Suddaby 1971), following new magma replenishment. However, more recently, it has been proposed that the ELI Cr-spinel seams crystallised in situ (Bédard et al. 1988), due to assimilation of the troctolite footwall by picritic melt

(O’Driscoll et al. 2009b; 2010). Variations of this model have subsequently gained traction for PGE-reef petrogenesis more generally; e.g. the Bushveld Complex chromitites (Latypov et al. 2013; 2015; 2017b).

## Field relations

The Unit 7–8 boundary was mapped and sampled in a number of localities across the extent of the ELI to assess lateral variation, with respect to distance from the inferred feeder zone in the centre of the intrusion (i.e., the Long Loch Fault; LLF; Emelcus et al. 1996; Volker and Upton 1990), of the Cr-spinel seam and its immediate footwall and hanging wall rocks (see Fig. 1 for locality details). In very general terms, the Unit 7–8 boundary sequence comprises the Unit 7 troctolite footwall with elongated anorthosite autoliths and peridotite schlieren both ubiquitous in the near vicinity of the contact (1–3 m), overlain by a 1–20 cm thick layer of anorthosite, the 1–3 mm thick main Cr-spinel seam and the Unit 8 feldspathic peridotite on top (Fig. 2a). However, from one locality to the next, significant structural and lithological variations are observed along strike.

The main Cr-spinel seam varies in thickness along strike (0.5–4 mm) with an average thickness ranging between 1 and 2 mm. It is generally located at the anorthosite–peridotite contact (Fig. 2a). However, the main seam may also locally transgress into the overlying peridotite (Fig. 3a, b). The Cr-spinel seam is undulose and frequently forms small depressions extending into the footwall (Fig. 2b), forming concentrated pockets of Cr-spinel (Fig. 3b, c). These structures were referred to as ‘cone-structures’ by O’Driscoll et al. (2010). The cones are usually 1–2 cm in width, but can reach amplitudes of up to 10 cm and it is reasonable to suggest they represent small-scale analogues of the so-called ‘potholes’ that frequently occur in the chromitite layers of the Merensky Reef and UG2 chromitite of the Bushveld Complex. The main seam is often accompanied by additional seams occurring within or at the lower contact of the anorthosite layer (Figs. 2c, d and 3d). These subsidiary seams can be oriented parallel to the main seam (Fig. 2c), or may bifurcate (Figs. 2e). They are generally thinner (0.5–1 mm) than the main seams and are often laterally discontinuous. Subsidiary seams within the anorthosite layer may occur in contact with thin peridotite apophyses (Figs. 2c and 3d). These apophyses are mm-thick, sheet-like or lensoid in form and are completely surrounded by a rind of Cr-spinel (e.g., Fig. 3d). The apophyses typically extend laterally over tens of centimetres. However, in some localities (such as Locality 12), the apophyses can be traced over distances of tens of metres. The footwall anorthosite layer below the main seam is a 2–20 cm thick (on average ~6 cm), strongly foliated layer that overlies the Unit 7 troctolite. The

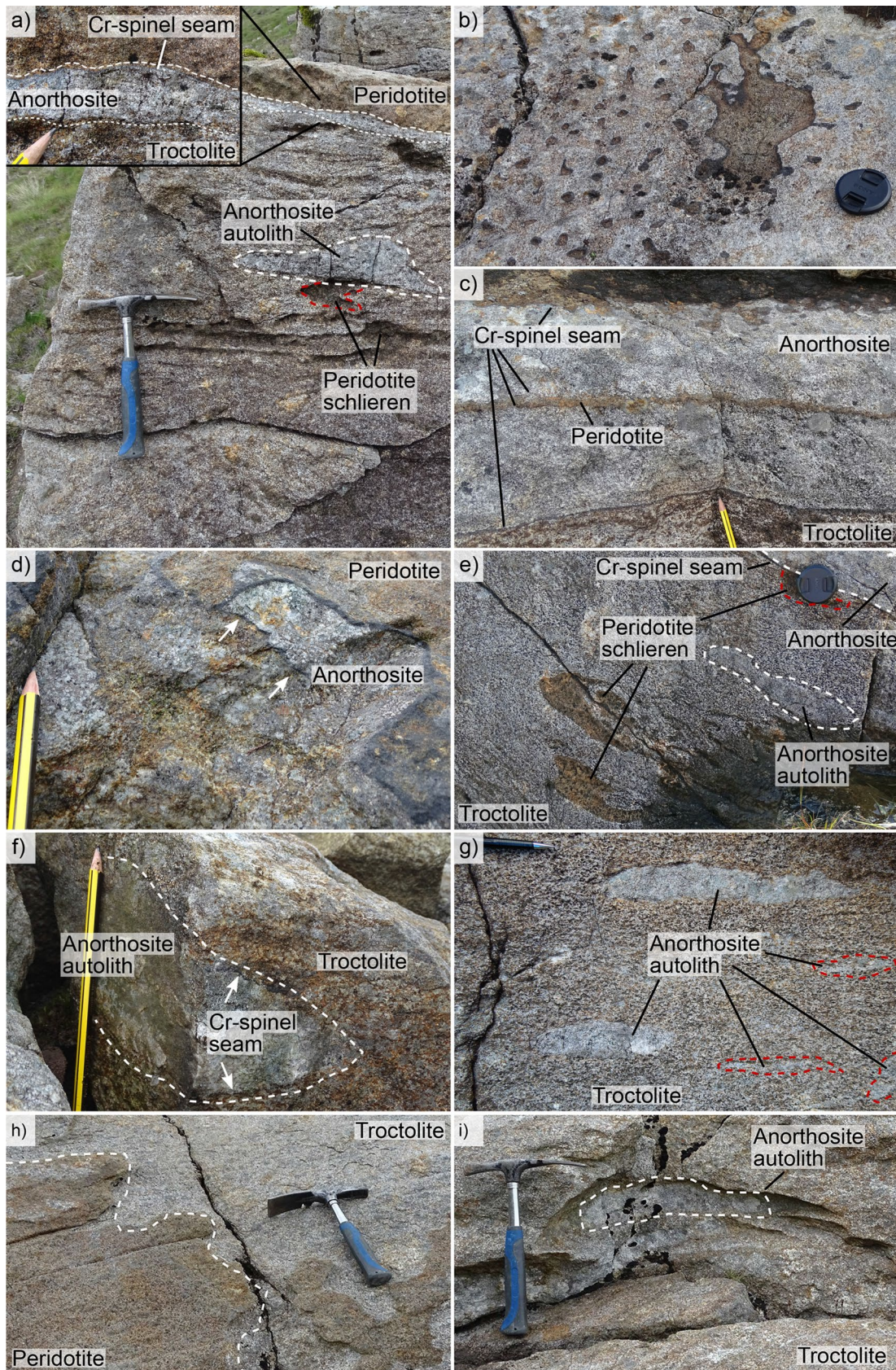


**Fig. 2** Field relations of the Unit 7–8 boundary. **a** Typical Unit 7–8 boundary with ca. 2 mm thick undulating Cr-spinel seam. Note that the anorthosite autoliths can be cross-cut by the peridotite schlieren, here marked in red (*Locality 13*). **b** Plan view of Cr-spinel seam. The seam forms small depressions extending into anorthosite (*Locality 1*). **c** Complex Unit 7–8 boundary with thick anorthosite layer, a layer of peridotite and four Cr-spinel seams, which occur on all contacts (*Locality 12*). **d** Bifurcation of Cr-spinel seam, additional small seam is indicated by arrows (*Locality 6*). **e** Unit 7 troctolite footwall troctolite with lengthened anorthosite autolith and deformed peridotite schlieren, which can be cross-cut by the anorthosite layer, here marked in red (*Locality 1*). **f** Anorthosite autolith (dashed lines) in the footwall troctolite rimmed by small Cr-spinel seams (arrows). **g** Anorthosite autoliths with smaller, irregular patches of anorthosite (*Locality 1*). **h** Unit 7–8 boundary without Cr-spinel seam and anorthosite layer (*Locality n 11*). **i** Anorthosite autolith (dashed lines), in place where the anorthosite layer is absent (*Locality 11*)

anorthosite layer is present in most of the boundary sections studied, but locally it is apparently cut or pinched out by the overlying Cr-spinel seam and hanging wall peridotite (Fig. 3a, b).

At distances greater than 3 m below the anorthosite, the Unit 7 troctolite is relatively undeformed and exhibits mesocumulate texture. Immediately below the anorthosite layer (uppermost 1–3 m), the footwall troctolite comprises a complex package of deformed cumulates containing highly deformed diffuse schlieren of peridotite. The basal contact of the overlying anorthosite layer cross-cuts the foliation, structures and peridotite schlieren in the troctolite (Fig. 2e). Autoliths of anorthosite commonly occur throughout the upper 3–5 m of the troctolite (Fig. 2a), with the exception that they are not seen in the uppermost 5–10 cm immediately below the anorthosite layer. The autoliths are elongate and generally lie with their long-axis (as observed on the outcrop plane) oriented parallel to layering in the troctolite, forming oblate ellipsoidal geometries. Some autoliths exhibit sigmoidal shapes, suggesting that they have been deformed with a component of simple shear indicating a top-down-to-the-west sense of movement. They vary in length from several mm to almost 0.5 m. The vertical (short) axis of the anorthosite autoliths rarely exceeds 10 cm and most are in the range of 1–5 cm. A systematic change in shape or aspect ratio depending on the distance to the anorthosite–troctolite boundary is not apparent. Some anorthosite autoliths are rimmed by mm-thick rinds of Cr-spinel (Fig. 2f). In addition to the well-defined autoliths, smaller, irregularly shaped patches of anorthosite are common in the footwall troctolite (Fig. 2g). These patches are typically elongated along the main troctolite layering too; however, their boundaries are more diffuse compared to the better defined autoliths.

The Unit 7–8 boundary is well-exposed along the Barkeval–Hallival traverse and can be mapped continuously over large parts of the northern portion of the ELI (Fig. 1). The seam in the localities to the northwest, close to Barkeval (Localities 6 and 7; Fig. 3c), displays the maximum

thickness (i.e. up to 4 mm), while it generally thins out towards the northeast (Fig. 4). To the north of Barkeval at a locality closer to the LLF, the seam is absent (Locality 15). Distal to the LLF, east and south of Hallival, exposure of the Unit 7–8 boundary is relatively poor but the main seam also appears to be absent (e.g., at Localities 11 and 17; Fig. 1). There are other significant variations observed in the Unit 7–8 package across the entire traverse. For example, the anorthosite layer appears to be relatively thick in the central part north of Hallival (> 10 cm), but thins out to < 1 cm thick in the northwest (i.e. Localities 6, 7, 13 and 14) and disappears entirely in the southeast (Locality 11 and further south; Figs. 2h and 3e). At its thickest, the lower contact of the anorthosite layer is bounded by a subsidiary seam (Localities 4 and 12), which can be traced for several tens of metres. To the northwest of Barkeval, exposure is poor and the subsidiary Cr-spinel seam and anorthosite layer are missing or are highly discontinuous. At Locality 15, the Unit 7 troctolite is directly overlain by the Unit 8 peridotite (Fig. 1). Here, the basal peridotite contact has an irregular topology, but crosscuts the foliation of the underlying deformed troctolite. Peridotite schlieren and anorthosite autoliths occur in the topmost 1–3 m of the Unit 7 troctolite across the entirety of the traverse regardless of the presence of the anorthosite layer and Cr-spinel seam (e.g., Fig. 2a, i). Systematic lateral variations in the distribution frequency or size of autoliths are not evident. Autoliths rimmed by Cr-spinel rinds are observed at several localities (e.g., Localities 6 and 11).

## Petrography

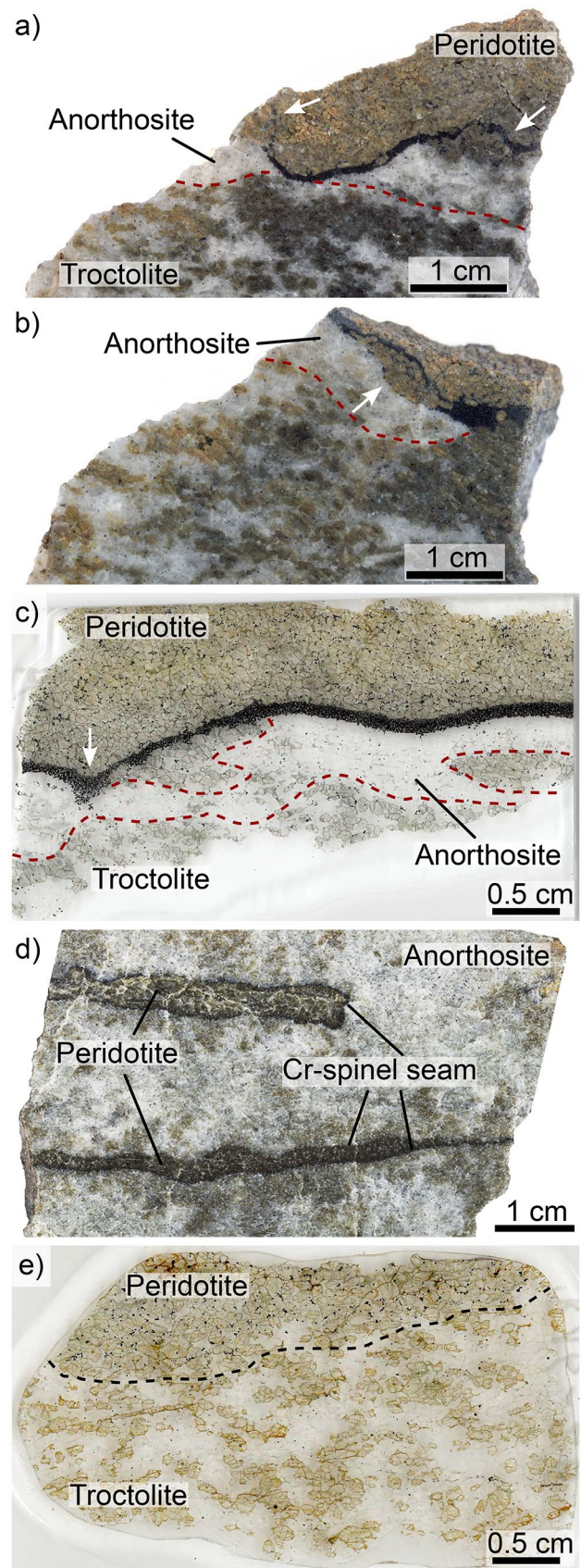
The granular-textured Unit 8 peridotite comprises euhedral (cumulus) olivine, euhedral Cr-spinel and intercumulus plagioclase and clinopyroxene (Fig. 3c, e). In general, Cr-spinel is embedded in the intercumulus plagioclase, often in well-developed embayments in olivine crystals (Fig. 5a). Less commonly, Cr-spinel occurs as inclusions in clinopyroxene or olivine crystals. In the lowermost 1–5 cm of the peridotite, diffuse concentrations of Cr-spinel are locally developed in a chain-textured arrangement around the cumulus olivine framework. The proportion of Cr-spinel in the Unit 8 peridotite ranges between 1 and 7 vol.%, with an average of ~3.5 vol.%.

Cr-spinel in the main seam is euhedral to subhedral, with a grain size range of 0.01–0.5 mm (average ca. 0.15–0.25 mm). The overall proportion of Cr-spinel in the seam ranges between 55 and 65 vol.%. Cr-spinel seams are typically cemented by intercumulus plagioclase and to a lesser extent (towards the tops of seams) by intercumulus olivine oikocrysts (Fig. 5c). Cr-spinel often forms clusters or chains of several crystals, attached by shared grain boundaries. Cr-spinel in these clusters is

**Fig. 3** **a** Wavy Cr-spinel seam cross-cuts the underlying anorthosite and migrates into the overlying peridotite (white arrow). **b** Main seam in the Unit 8 peridotite, a small additional seam occurs at the peridotite/anorthosite contact (white arrow). **c** Typical thin-section of the Unit 7–8 boundary with Cr-spinel seam (*Locality 6*), with a thickened Cr-spinel cone (white arrow). **d** Two peridotite apophyses in the anorthosite layer, both are rimmed by a small Cr-spinel seam (*Locality 12*). **e** Thin-section scan of the Unit 7–8 boundary without Cr-spinel seam and anorthosite layer (*Locality 11*)

coarser grained than disseminated crystals. Plagioclase from the underlying anorthosite layer and olivine from the overlying peridotite extend into the seam (Fig. 5a, c), as indicated by optical continuity of these minerals across the seam boundaries. Thus, a given olivine or plagioclase crystal can be partly primocrystic and partly intercumulus. As with accessory Cr-spinel in the peridotite, main seam Cr-spinel is typically situated in embayments in olivine where both phases are in close proximity (i.e. at seam edges; Fig. 5a, e). Cr-spinel in the thinner subsidiary seams and in rinds around anorthosite autoliths is petrographically similar to that in the main seam (Fig. 5b). Base metal sulphides (BMS) occur in all varieties of Cr-spinel seams (Fig. 5f). The BMS crystals are typically situated in contact with the edges of one or more Cr-spinel crystals. More rarely, the BMS occur as rounded inclusions in Cr-spinel crystals. They vary in size (0.01–0.1 mm), but are typically in the range of ca. 0.3–0.5 mm.

The anorthosite layer below the Cr-spinel seam is composed of strongly aligned plagioclase (Fig. 5d) and variable proportions of intercumulus olivine (0–15 vol.% with an average of 10 vol.%). Although this would technically classify some of these rocks as leucotroctolite, we retain the term anorthosite for these rocks to be consistent with the previous literature (e.g., Bédard et al. 1988; O’Driscoll et al. 2009b). Cr-spinel is ubiquitous (up to 4 vol.%, with an average of 2.5 vol.%) in the layer. Plagioclase crystals are blocky to tabular and aligned parallel to the upper and lower contacts of the anorthosite layer. Plagioclase grain-size varies from 0.1 to 2 mm (long axis), with an average size of 0.25 mm. Compositional zoning is a common feature in these plagioclase crystals, ranging from distinct core-rim zonation to irregular patchy zoning (Fig. 5d). In many respects, the anorthosite autoliths are petrographically similar to the anorthosite layer. Both comprise foliated plagioclase crystals, which are aligned parallel to the long axis of the autoliths; however, plagioclase in the autoliths is often cemented by interstitial hornblende or clinopyroxene, instead of olivine. Plagioclase grains in the anorthosite layer and autoliths are notably finer grained directly adjacent to the contact with the host troctolite. Plagioclase in the autoliths has strongly developed compositional zoning, in most cases normal zoning. Cr-spinel is less frequent in



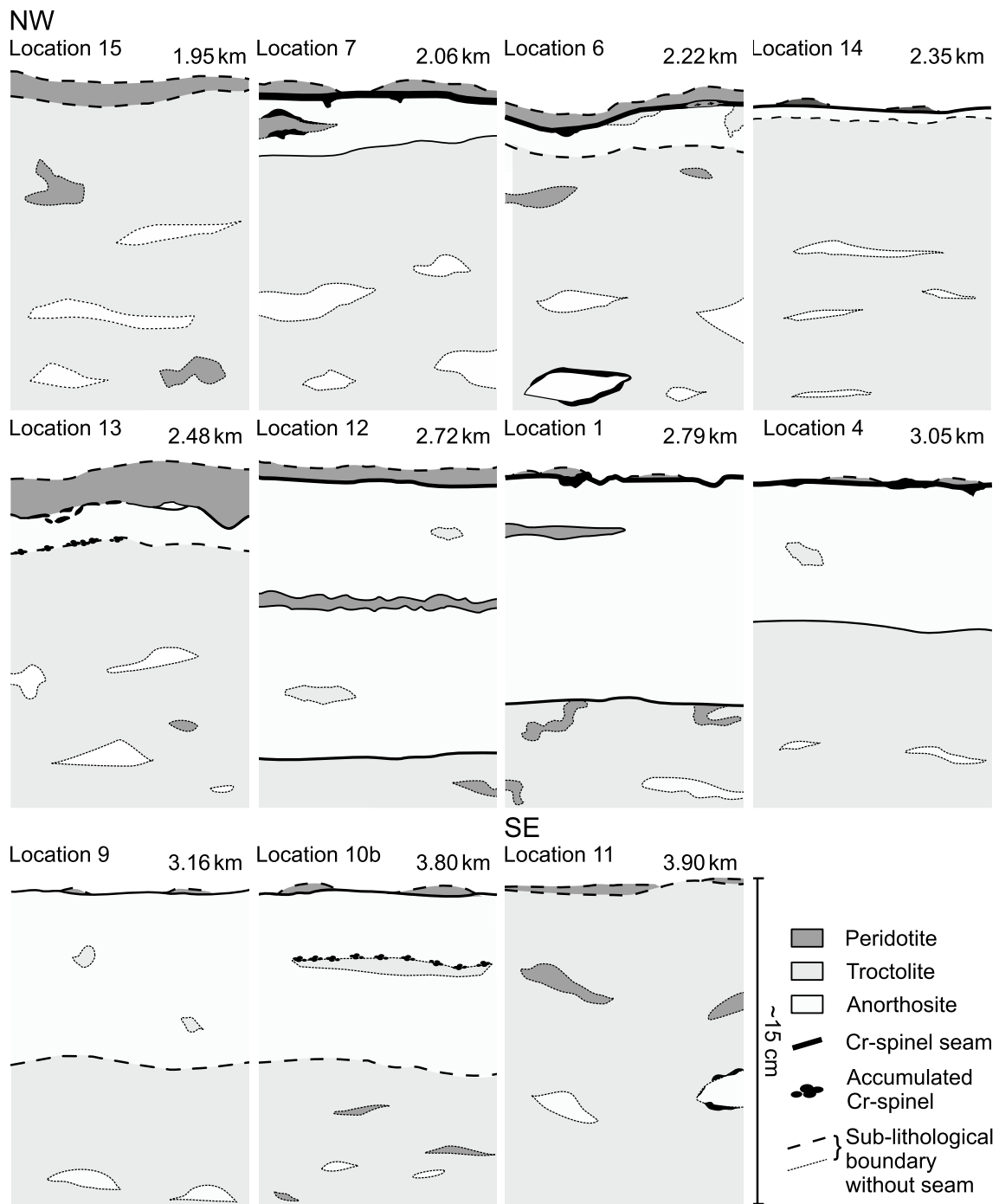


**Fig. 4** Sketches of the Unit 7–8 boundary zone along strike, for sample location see Fig. 1. Distance to the Long Loch Fault (LLF), measured as the shortest distance to the LLF is given for each panel in the

upper right corner. Locality 4 is the ‘classic outcrop’ described in by e.g. Young 1984, O’ Driscoll et al. 2009b; O’Driscoll et al. 2010, Locality 12 has been described by Bédard et al. (1988)

the autoliths relative to the massive anorthosite layer, with typical proportions of ~1 vol.%. Apatite is a local accessory phase.

In the 1–3 m of stratigraphy below the anorthosite layer, the Unit 7 troctolite comprises unevenly distributed clusters of olivine and plagioclase (Fig. 3e). Plagioclase forms

tabular laths that are oriented parallel to the layering. Olivine crystals are typically equant to tabular in shape. The plagioclase crystals are normally zoned, but this is less well-developed compared to plagioclase in the anorthosite layer and autoliths. Intercumulus clinopyroxene oikocrysts occur close to olivine-rich portions of the troctolite. Disseminated

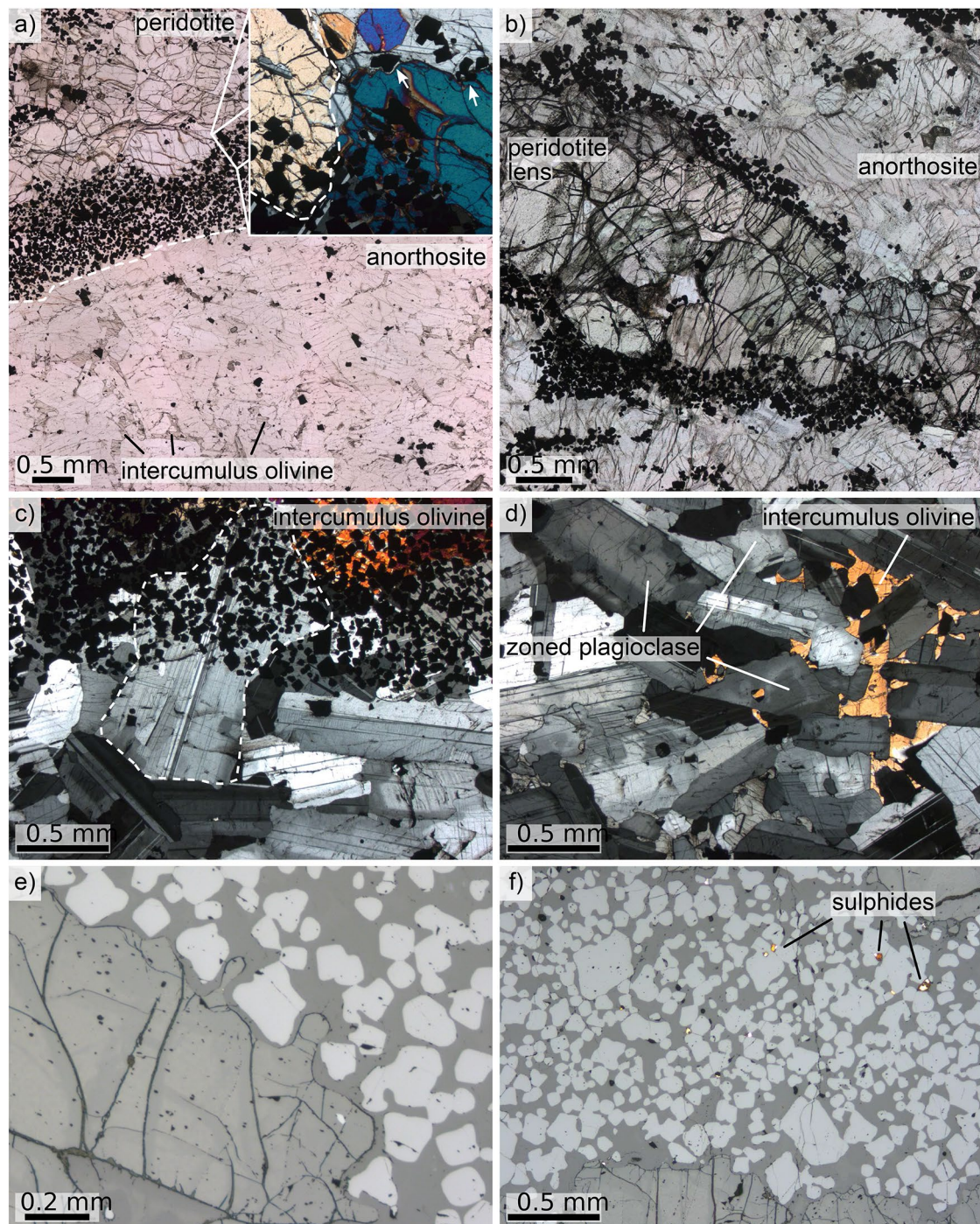


**Fig. 5** Photomicrographs in plane and crossed polarised light. **a** Plane polarised light image of a typical Unit 7–8 Cr-spinel overlain by peridotite and underlain by the anorthosite layer, the Unit 7–8 boundary is indicated by a dashed line. Inset shows olivine primocrysts extending into the underlying Cr-spinel seam (indicated by dashed line) and the occurrence of Cr-spinel in embayment structures in olivine above the seam (highlighted by arrows). **b** Peridotite schlieren in the

Cr-spinel appears throughout the troctolite, but is less common (~0.7 vol.%) than in the anorthosite layer and the Unit 8 peridotite. Locally, hornblende is observed as an accessory

anorthosite layer, surrounded by a Cr-spinel rind. **c** Crossed polarised light photomicrograph of plagioclase primocryst extending into the overlying Cr-spinel seam, indicated by dashed line. **d** Anorthosite layer below the Unit 7–8 seam with foliated plagioclase primocrysts and interstitial olivine. **e** Embayment structure of Cr-spinel into an olivine crystal. **f** Association of BMS crystals in the Cr-spinel seam

phase. At > 3 m below the troctolite–anorthosite contact, plagioclase zoning and preferred alignment are less common in the Unit 7 troctolite.

## Analytical techniques

### Quantitative fabric analysis

Quantitative textural analysis was carried out on the plagioclase primocrysts in the Unit 7–8 boundary package to compare and evaluate the microstructural character of this phase in the anorthosite lithologies compared to the host troctolite. To quantify the strength of the foliation in the troctolite, anorthosite layer and autoliths, between 200 and 450 (average 280) plagioclase primocrysts were outlined in digitised photomicrographs in crossed polarised light for four localities (6, 13, 4 and 11, Fig. 1). The major and minor axis length, orientation and spatial distribution were measured using the program ImageJ. Average aspect ratios were calculated using the major and minor axis lengths. Plagioclase crystal alignment estimates in the samples were obtained using CSDCorrections 1.5 by Higgins (2000), which quantifies an alignment factor, ranging from 0 (no statistically significant alignment) to 1 (perfect alignment of grains) (see Meurer and Boudreau (1998) and Boorman et al. (2004) for further information). We used the normalised grainsize frequency of the length (i.e. major axis) and width (i.e. minor axis) of plagioclase to calculate the apparent grain size distribution, following the approach described by Holness (2014) and Holness et al. (2017). While most of the sections were prepared perpendicular to the foliation, three additional sections from Locality 6, one for the troctolite, one for the anorthosite layer and one for an anorthosite autolith, were cut parallel to the foliation. These sections were utilised to quantify crystal size, aspect ratio and lineation strength within the foliation plane for these samples.

### Mineral chemistry

The mineral chemistry of plagioclase, olivine and Cr-spinel in the Unit 7–8 package of rocks was investigated by electron microprobe (EMP) and LA-ICP-MS for five different localities (7, 6, 13, 10b and 11; Fig. 1). These included one of the localities without a Cr-spinel seam (Locality 11). These measurements were conducted to assess if and how the presence of the Cr-spinel seam and anorthosite layer controls the mineral chemistry of the main phases and to potentially link the lateral variations observed in the field with potential compositional differences in the constituent minerals of the Unit 7–8 boundary package.

EMP analyses were carried out at the Museum für Naturkunde Berlin on a JEOL JXA-8500F EMP equipped with a field emission cathode and five

wavelength-dispersive spectrometers. Cr-spinel, olivine and plagioclase were analysed with the following conditions: 20 kV accelerating voltage for Cr-spinel and 15 kV for olivine and plagioclase measurements, 20 and 15 nA beam current for Cr-spinel and olivine and plagioclase, respectively. The spot size was set to 1  $\mu\text{m}$  for Cr-spinel and olivine, with a defocused beam spot size of 5  $\mu\text{m}$  for plagioclase to minimize the effect of alkali loss. The measured intensities were calibrated against natural minerals of the Smithsonian international standard suite (Jarosewich et al. 1980) and pure metals of the Astimex metal standard. Analyses were processed by a ZAF routine by the JEOL series operating system to minimise matrix effects. Accuracy and reproducibility were checked regularly before and after each analysis session by measurements on minerals of the Smithsonian mineral standards (Cr-spinel, USNM 117,075; Olivine San Carlos, USNM111312/444; Olivine Springwater meteorite, USNM 2566; Anorthite, USNM 137031; Anorthoclase, USNM 133868, Microcline, USNM 143966, Jarosewich et al. 1980). The ferric iron contents of Cr-spinel were calculated assuming ideal stoichiometry (Droop 1987).

LA-ICP-MS analyses for trace element concentrations in olivine and plagioclase, focusing on the distribution of the rare-earth elements (REE) in the latter, were performed at the Institut für Mineralogie of the Leibniz Universität Hannover (LUH) with a fast scanning-sector field-ICP-MS (ThermoScientific ElementXR) which is connected to a femtosecond (Ti-sapphire) laser ablation system. Further details of the fs-LA system are given in Oeser et al. (2014) and Lazarov and Horn (2015). In our study, the laser operated at 30–40 Hz and the spot size was set to 40–50  $\mu\text{m}$  diameter. Most analyses were performed in raster mode, but the rims of plagioclase grains were ablated in line mode. Acquisition times of the background signal and the ablation signal were set to 40 s and 100 s, respectively. To avoid artefacts due to surface contamination, sample surfaces of each spot were pre-ablated before measurement. Analyses were bracketed every 10–15 measurements by the standard reference material NIST610 to correct for internal instrumental drift. Further testing of the accuracy and reproducibility was undertaken by measuring silicate reference material (BCR-2G), which yielded an accuracy and reproducibility of 1–5%. Silicon concentrations, obtained by EMP analyses, were used for the internal calibration of trace element concentrations for plagioclase and olivine. Data processing was performed with the SILLS program (Guillong et al. 2008).

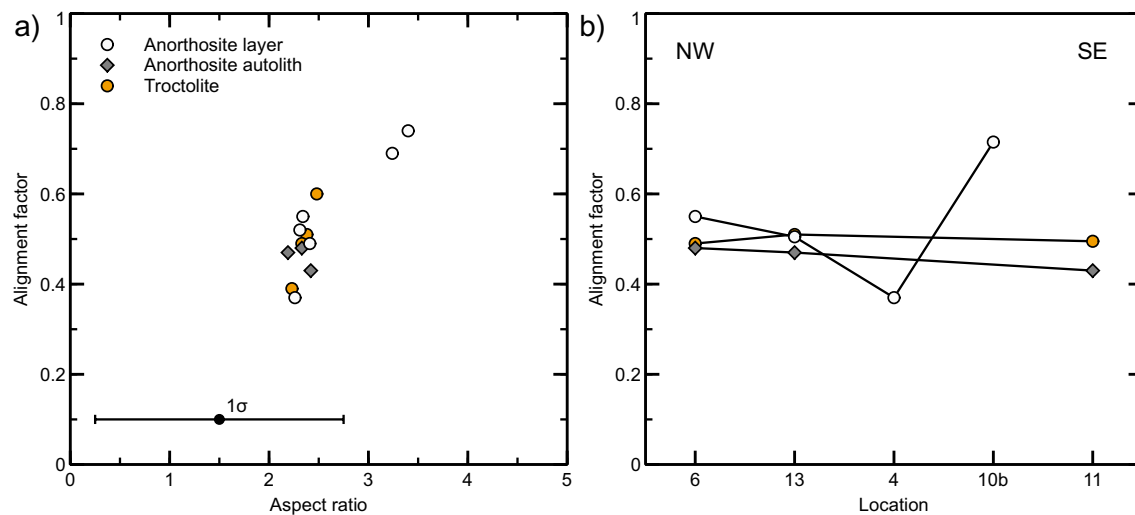


**Fig. 6** **a** Alignment factor against aspect ratio of plagioclase primocrysts (Localities 4, 6, 10b, 11 and 13) in the anorthosite layer, autoliths and troctolite, the average standard deviation illustrated is

representative of the combined dataset. One data point represents on average 280 plagioclase crystals. **b** Development of alignment factor of plagioclase along strike, for sample location see Fig. 1

## Results

### Quantitative fabric analysis

Plagioclase primocrysts in the anorthosite layer, anorthosite autoliths and the troctolite exhibit similar microstructural characteristics, based on the thin sections cut perpendicular to the foliation. Average aspect ratios of plagioclase in both types of anorthosite and the troctolite range between 2.2 and 2.5, with alignment factors that mostly range between 0.4 and 0.6 (Fig. 6a). Two outliers from the anorthosite layer plot at higher aspect ratios and alignment factors. The data are positively correlated, such that aspect ratios and alignment factors increase systematically. Across the lateral extent of the Unit 7–8 boundary, plagioclase in the anorthosite autoliths and the troctolite exhibits relatively constant alignment factors (Fig. 6b). Plagioclase fabric in the anorthosite layer is more variable, with a relatively low alignment factor observed at Locality 4 and a relatively high alignment factor at Locality 10b; the latter locality is close to the southeastern termination of the anorthosite layer. The aspect ratios of plagioclase in thin sections cut parallel to the foliation plot in the same range, although values are slightly smaller (1.9 and 2.1, respectively), while alignment factors are significantly lower (0.05 and 0.15, respectively), suggesting that there is little or no lineation present in any of the samples (Fig. S1). Grainsize frequency distributions (Fig. 7) for plagioclase (both long and short axes) measured perpendicular to the foliation are unimodal with a broader peak at 0.25 mm crystal length and a well-defined narrow peak at 0.15 mm crystal width. The plagioclase from the anorthosite layer, the anorthosite autoliths and the troctolite all show

similar grain size distributions. In addition, the grain size is unaffected by the orientation. Plagioclase grain size frequencies in sections prepared parallel to the foliation are similar to those described above (see Fig. S2).

### Mineral chemistry

#### Cr-spinel

The Rum Cr-spinel compositional range can broadly be subdivided into Cr-Al-dominated and Cr-Fe<sup>3+</sup>-dominated varieties (Fig. 8; Table. S1). Cr-spinel in peridotite, Cr-spinel seams and troctolite are Cr-Al dominated spinels, following the so-called ‘Rum trend’ (Henderson 1975). Cr-spinel compositions in the anorthosite layer and anorthosite autoliths are Cr-Fe<sup>3+</sup> dominated and follow the Fe-Ti-trend of Barnes and Roeder (2001). Cr-spinel exhibits a range of Mg# (atomic ratio Mg/(Mg + Fe<sup>2+</sup>) × 100) of between 2 and 72 and Cr# (atomic ratio Cr/(Cr + Al) × 100) from 22 to 82 (Fig. 9). Anorthosite-hosted Cr-spinel generally has lower Mg# and higher Cr# relative to Cr-spinel in the other lithologies. Cr-spinel in the seams exhibits lower Cr# and higher Mg# compared to other lithologies. Cr-spinel TiO<sub>2</sub> concentrations range between ~0.2 and 6.2 wt.%. The Cr-spinel from Locality 11 has relatively elevated TiO<sub>2</sub> contents, with concentrations of up to 6.2 wt.% in the troctolite, compared to localities that contain a Cr-spinel seam. Anorthosite Cr-spinel compositions vary depending on whether the crystals occur in the anorthosite layer or the autoliths within the Unit 7 troctolite. Specifically, Cr-spinel crystals in the autoliths have elevated TiO<sub>2</sub> contents and generally lower

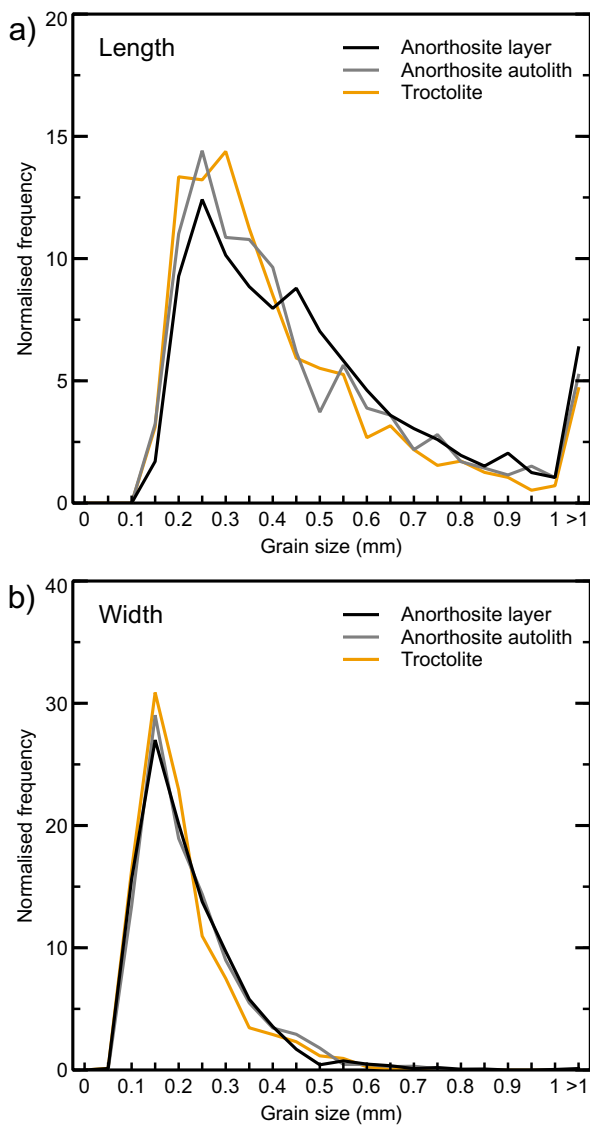


**Fig. 7** Normalised frequency plot for (a) long and (b) short axes of plagioclase primocrysts (Localities 4, 6, 10b, 11 and 13) in the anorthosite layer, autoliths and troctolite

Mg#. Traverses across the main Cr-spinel seam indicate that Cr-spinel within the seam is characterised by a slight decrease in Mg# ( $\Delta$ Mg# 3–6 mol.% difference), which is mirrored by a slight increase in Cr# ( $\Delta$ Cr# 4–8 mol.% difference) towards the top of the seam (Fig. S3). Similar intra-seam compositional variations have been reported for the Unit 7–8 and Unit 11–12 Cr-spinel seams (O’Driscoll et al. 2009b, 2010), as well as for Cr-spinel seams of the Unit 10 peridotite (Hepworth et al. 2017). The lower contact of the seam to the anorthosite layer is characterised by an abrupt compositional change towards lower Mg# and higher Cr#, while the contact of the overlying peridotite shows a smoother transition for both values (Fig. S3).

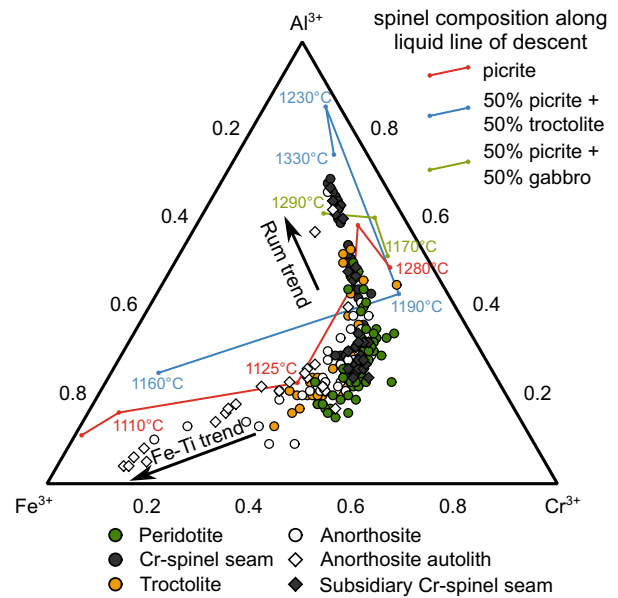


**Fig. 8** Trivalent cation ( $\text{Al}^{3+}$ - $\text{Cr}^{3+}$ - $\text{Fe}^{3+}$ ) ternary plot for Cr-spinel, Run trend and Fe-Ti Trend (Barnes and Roeder 2001; Henderson 1975) are indicated by arrows. Averaged experimental data on spinel equilibration along liquid line of descent at 0.1 MPa and QFM for picritic and hybrid melts are taken from Leuthold et al. (2015)

Cr-spinel compositions in the main Cr-spinel seam reveal a systematic change along strike (Fig. 9). Cr# and  $\text{TiO}_2$  concentrations increase while Mg# decreases with increasing distance from the central part of the intrusion, i.e. towards the SE and away from the LLF (from Locality 7 to 11; Fig. 1). Importantly, these compositional changes exceed the vertical variations across different profiles. Cr-spinel in peridotite, the main seam and in anorthosite in Locality 13 displays a broader compositional scatter and relatively high Cr# and  $\text{TiO}_2$  concentrations and lower Mg# values, compared to other localities. Locality 13 differs in comparison to the other localities in that the Cr-spinel seam is very diffuse, and the Unit 8 peridotite is cemented by clinopyroxene and plagioclase instead of plagioclase alone.

## Olivine

Olivine Mg# compositions range between 82 and 90, with Ni concentrations of 1400–2600 ppm (Fig. 10; Table. S2). No compositional zoning was observed in olivine from any lithology, in either the primocrysts or in the intercumulus crystals. Olivine in peridotite has slightly higher Ni concentrations and generally shows a broader scatter compared to olivine in the troctolite and interstitial olivine in the anorthosite layer. Olivine in the anorthosite has similar Mg# values, but lower Ni concentrations, compared to olivine in peridotite and troctolite, an observation also made by O’Driscoll et al. (2009b). LA-ICP-MS analyses confirm the

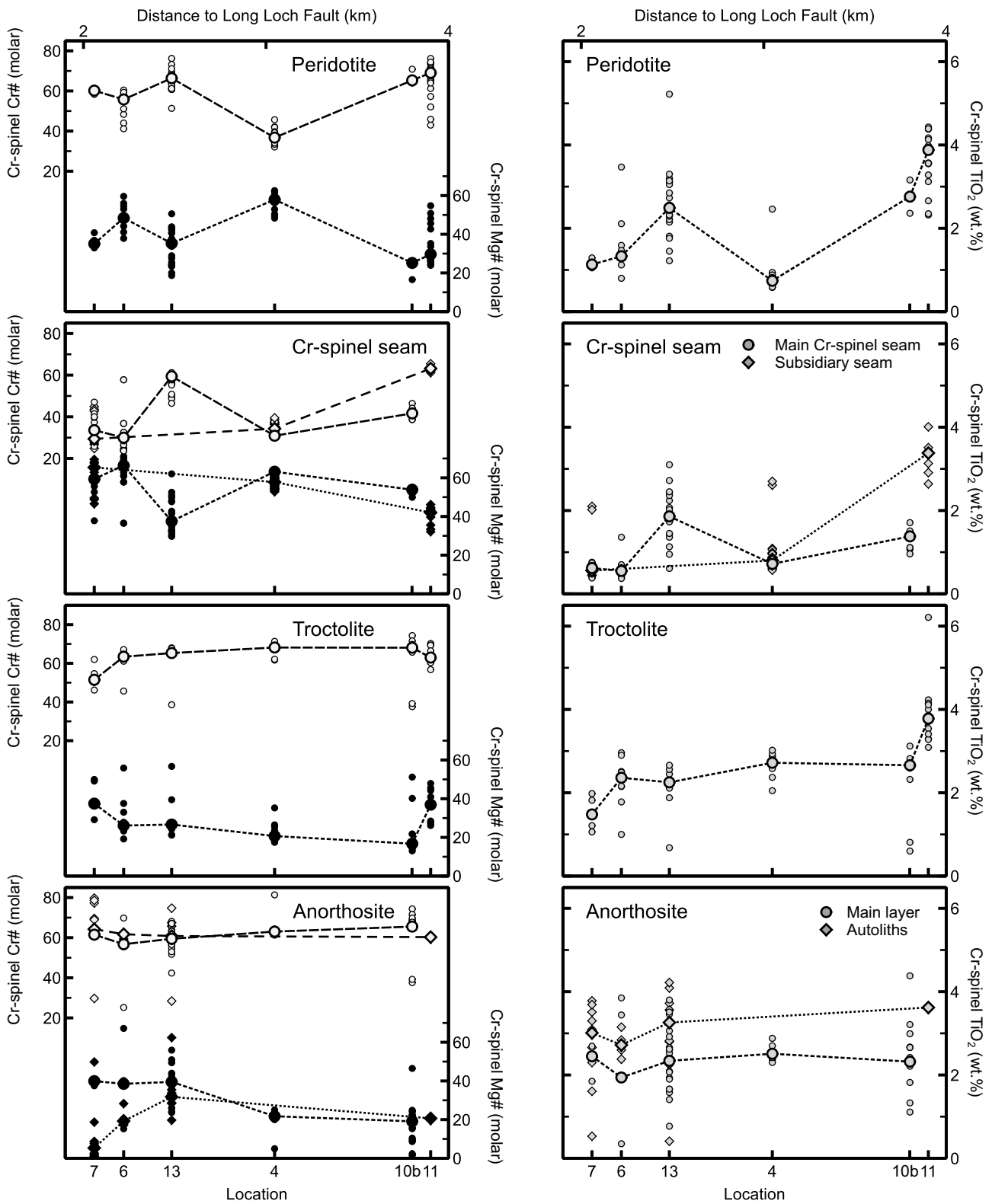


**Fig. 9** Variation in Cr-spinel composition against distance to the LLF. Data for Locality 4 were taken from O’Driscoll et al. (2009b). Cr-spinel in the seams shows lower Cr# and higher Mg#, while anorthosite-hosted Cr-spinel has generally lower Mg# and higher Cr# compared

to the other lithologies. In addition, Cr-spinel compositions in the main Cr-spinel seam reveal a systematic change along strike with increasing Cr# and TiO<sub>2</sub> concentration while Mg# decreases with increasing distance to the LLF

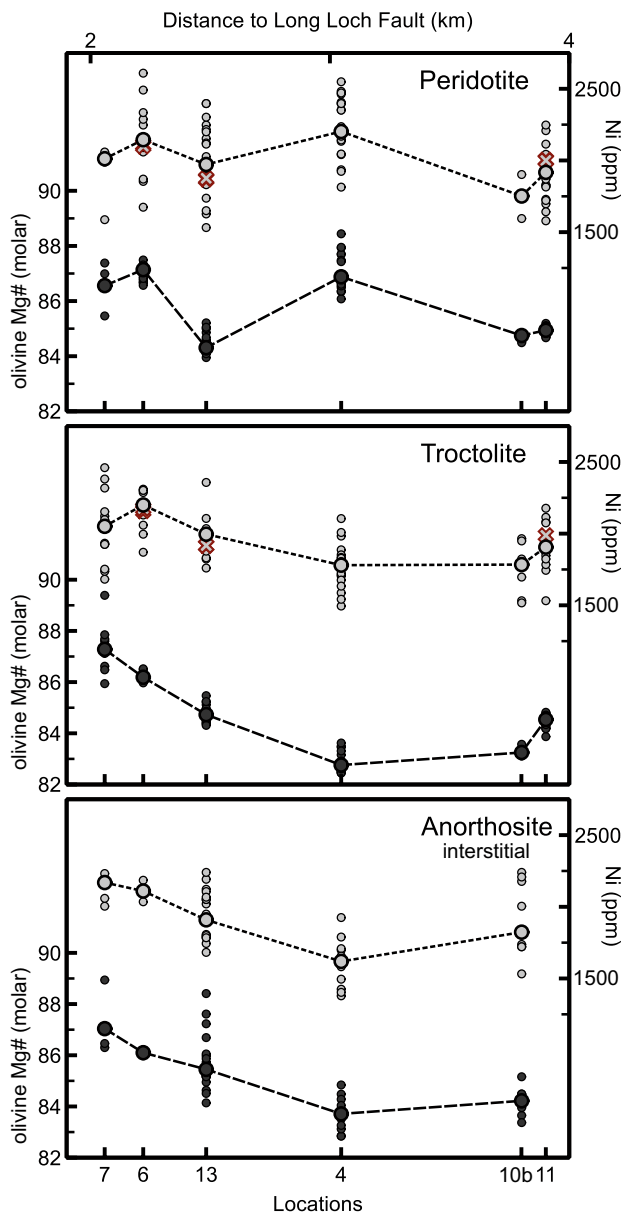


**Fig. 10** Variation in olivine composition against distance to the LLF, measured with EMP (circle) and LA-ICP-MS (red cross). Data for Locality 4 were taken from O'Driscoll et al. (2009b). Olivine in peridotite shows a broader compositional scatter compared to olivine in the troctolite and anorthosite, which show a systematic decrease in Mg# and Ni concentrations along strike

trace element concentrations measured by EMP. A consistent lateral change in olivine composition is observed along the strike of the Unit 7–8 boundary package for interstitial olivine in anorthosite. Specifically, Mg# and Ni concentrations in olivine in the anorthosite layer decrease with increasing distance from the central part of the intrusion towards the SE portion of the traverse (Fig. 10). Olivine in troctolite reveals a similar trend; however, the locality without a Cr-spinel seam (11) at the greatest distance from

the intrusion centre shows relatively high Mg# ( $\Delta\text{Mg\#} \approx 2$  mol.% difference over the traverse) and Ni concentrations ( $\Delta\text{Ni} \approx 100$  ppm over the traverse). In contrast, olivine in the Unit 8 peridotite shows no systematic lateral variations across the investigated traverse.

### Plagioclase

Compositional data of plagioclase cores are reported in Table S3 and illustrated in Fig. 11. Anorthite content in plagioclase (An) varies from  $\text{An}_{65}$  to  $\text{An}_{92}$  and K concentrations vary between being below detection limits to  $\sim 1250$  ppm. The plagioclase in peridotite and anorthosite typically has elevated K and Na, relative to the intercumulus plagioclase in the Cr-spinel seams and Unit 7 troctolite primocrysts. Plagioclase from all lithologies reveals a broadly common trend of decreasing Ti concentration with increasing An content. Overall, Ti contents in plagioclase range from 100 to 680 ppm in all lithologies. Plagioclase in autoliths and interstitial plagioclase in the peridotite displays a broader scatter in Ti and K concentrations, while plagioclase in troctolite and the Cr-spinel seam show less scatter. Additionally, plagioclase in the anorthosite layer and interstitial plagioclase in the main Cr-spinel seam also exhibit lateral compositional variation along strike, i.e. decreasing An contents and increasing K and Ti concentrations with increasing distance from the central part of the intrusion (Fig. 11). Although compositional heterogeneities in plagioclase were observed locally (including normal zoning), the general lateral compositional shift along strike exceeds locality-specific chemical variations. Plagioclase from Locality 13 displays a broad compositional scatter, with relatively low An and higher Ti and K concentrations in peridotite, anorthosite and the main Cr-spinel seam.

Compositional zoning in plagioclase primocrysts is common; crystals typically show a pronounced normal zoning with calcic cores and sodic rims enriched in minor and trace elements. Anorthite content in primocryst rims generally differs by 5–10 mol.%; however, single crystals can exhibit internal An heterogeneity of up to 20 mol.%. Core-rim differences of trace element concentrations range from  $\sim 500$  to 1000 ppm and  $\sim 200$  to 300 for Ti and K, respectively. In addition, intercumulus plagioclase in peridotite and in the Cr-spinel seams is occasionally zoned, showing similar trends, though less well developed compared to the zoning patterns observed in cumulus plagioclase ( $\Delta\text{An}$  of 2–3 mol.%).

The REE element patterns of plagioclase cores and rims from the different Unit 7–8 lithologies are shown in Fig. 12. The patterns suggest that plagioclase in all lithologies broadly spans the same range of REE concentrations; however, plagioclase in the anorthosite is characterised by a broader scatter. All patterns (normalised to the primitive B65

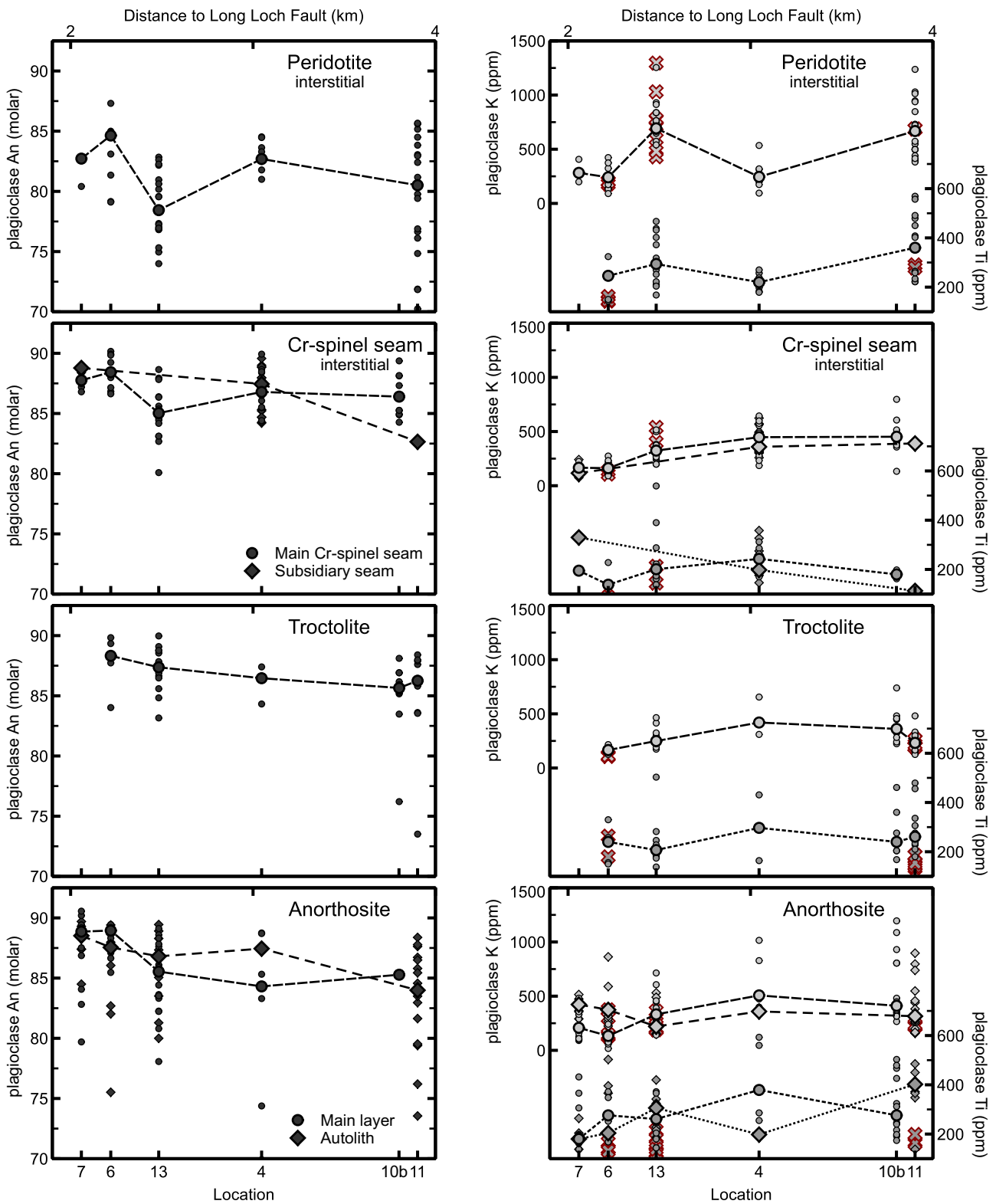


**Fig. 11** Compositional variations in plagioclase against distance to the LLF, measured with EMP (circle) and LA-ICP-MS (red cross) with additional data for Locality 4 (O’Driscoll et al. 2009b). Plagioclase in anorthosite typically has higher K and Na concentrations relative to interstitial plagioclase in the Cr-spinel seams and the pri-

mocrysts in the troctolite. Additionally, plagioclase compositions show lateral variation in the anorthosite layer and interstitially in the main Cr-spinel seam, which have lower An contents and higher K and Ti concentrations, with increasing distance to the LLF

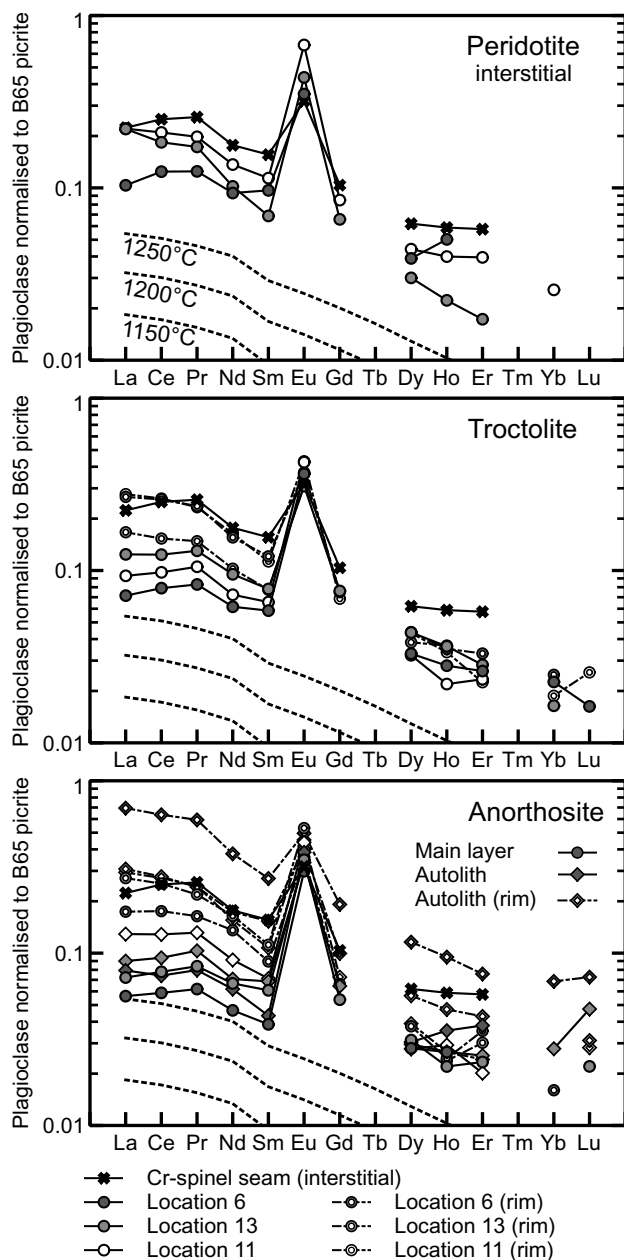


**Fig. 12** REE concentration of plagioclase normalised to the postulated parental magma B65 (Upton et al. 2002). Dashed lines depict calculated plagioclase composition in equilibrium with B65 for 1250, 1200 and 1150 °C, taken from Sun et al. (2017)

picrite of Upton et al. 2002) reveal relative enrichments in light REE (LREE) compared to heavy REE (HREE), similar slopes and strong positive Eu anomalies, most pronounced in plagioclase from the anorthosite layer. For comparison, we calculated the theoretical REE composition of plagioclase, which would crystallise in equilibrium from a parental magma B65 at 15 MPa (Holness 1999) and varying temperatures, using the partition coefficients of Sun et al. (2017). The calculated equilibrium patterns have lower overall REE

concentrations; however, their slopes are similar to the distribution of the data measured here (Fig. 12). REE concentrations decrease with decreasing temperatures. Plagioclase in the anorthosite autoliths is generally enriched in the REE compared to those in the anorthosite layer. In addition, both plagioclase in the anorthosite layer and autoliths exhibit enrichment in REE concentrations towards the southeast of the traverse with increasing distance from the centre of the intrusion. Thus, plagioclase in autoliths from Locality 11, east of Hallival, reveals the highest REE contents. Rims of zoned primocrysts in troctolite and anorthosite are relatively enriched in REE, compared to crystal cores; an observation that is most obvious in the plagioclase compositions from the anorthosite layer and autoliths. Although the level of core-to-rim enrichment is variable, some plagioclase crystals in the anorthosite have rims that are enriched by up to an order of magnitude, relative to their cores. Interstitial plagioclase in the Cr-spinel seams is relatively enriched in the REE compared to plagioclase primocrysts of the anorthosite layer.

## Discussion

### The origin of anorthosite in the Unit 7 troctolite

Anorthosite occurs in many well-known layered intrusions (see Ashwal 1993 for a general overview); in some cases like the Sept Iles layered intrusion, Canada, the Stillwater Complex, USA or the Bushveld Complex, considerable volumes of anorthosite are present. However, the petrogenesis and especially the timing of these rocks is still highly controversial (e.g., Mungall et al. 2016; Wall et al. 2018). Anorthosite layers are often accompanied by chromitites in layered intrusions; the UG1 anorthosite-chromitite association of the Bushveld Complex is a good example of this. Anorthosite layers commonly occur throughout the ELI (e.g., Brown 1956; Emeleus et al. 1996; Lenaz et al. 2011; Leuthold et al. 2014; Volker and Upton 1990), often in close association with the Cr-spinel seams, but their relationship to autoliths of anorthosite and the lateral variation of specific anorthosite layers has not been explored in detail before. Latypov et al. (2020) suggested that monomineralic anorthosites in the Bushveld Complex crystallised from melts that became plagioclase-saturated in response to pressure reduction of the ascending melt. However, their model is not applicable to the ELI, because their proposed melts are of basaltic composition, contrary to the picritic parental melts of the ELI. Therefore, the continuous anorthosite layer and the underlying anorthosite autoliths of the Unit 7–8 boundary package (Fig. 2) are discussed here in the context of their formation within the intrusion, as well as their links to the crystallisation of the Cr-spinel seams.

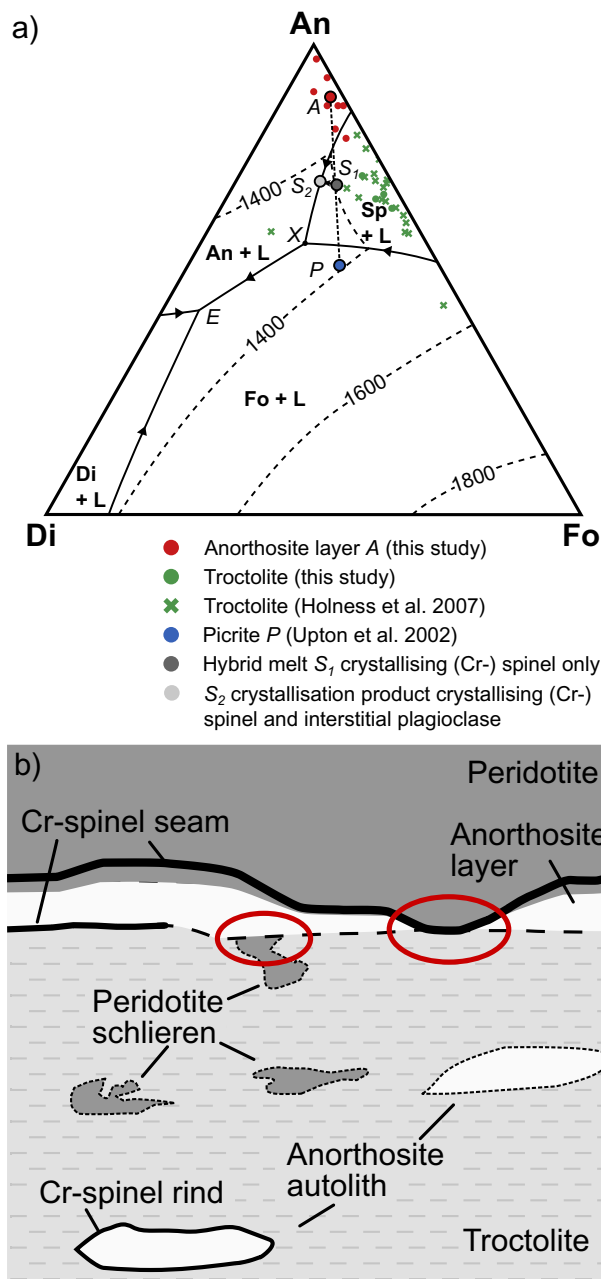


**Fig. 13** **a** Pseudo ternary phase diagram for the system olivine-plagioclase-clinopyroxene (Fo-An-Di), illustrating the reaction proposed for the formation of anorthosite and Cr-spinel. **b** Graphic compilation of the most important field evidence indicating a chronology for the formation of the Unit 7–8 boundary package. Straight lines represent Cr-spinel seams, while dashed lines indicate contacts without Cr-spinel

The anorthosite layer at the Unit 7–8 boundary was previously described and interpreted as a layer of partially dissolved troctolite (e.g., Bédard et al. 1988; O’Driscoll et al. 2009b, 2010). O’Driscoll et al. (2009b; 2010) suggested a model where infiltrating picritic melt dissolved the troctolitic cumulate, resulting in a restitic anorthosite layer.

Based on the pseudo-ternary forsterite-diospide-anorthite diagram (Fig. 13) and the experiments of Donaldson (1985), an infiltrating picrite could dissolve anorthite and olivine, resulting in a peritectic reaction and Cr-spinel crystallisation at point X (Morse 1980). We suggest that the peridotite schlieren throughout the top 3 m of the Unit 7 troctolite are evidence of this infiltration process. We thus consider the driving force for this reaction to have been thermochemical disequilibrium caused by open-system replenishment of picritic magma. Our new plagioclase mineral chemistry and microstructure data lend support to this model. Plagioclase in the anorthosite layer and the underlying troctolite have similar grain sizes (Fig. 7). A replacive origin, where olivine is completely resorbed, and existing cumulus plagioclase is concentrated to form anorthosite would produce such texture. Subsidiary seams, which have previously been interpreted as representing the lower limits of near-complete troctolite dissolution by O’Driscoll et al. (2010), are present in multiple localities along the Unit 7–8 traverse, supporting the intrusion-wide applicability of the infiltration model. We used our REE plagioclase data (Fig. 12) in combination with equilibrium crystallisation temperature calculations for plagioclase (following Sun et al. 2017) and whole-rock data (O’Driscoll et al. 2009a) to model the evolution of the anorthosite layer (see Fig. S4).

Our models show that the relatively elevated REE concentrations of plagioclase cores in the autoliths compared to calculated equilibrium crystallisation from a parental picrite magma, i.e. sample B65 of Upton et al. (2002), can be best explained by mixing of the picrite with partially melted troctolite. We chose the equilibrium crystallisation temperature of 1240 °C for the theoretical plagioclase REE pattern based on the experimental observations of Leuthold et al. (2015), who reported plagioclase saturation for picrite–troctolite melt mixtures at this temperature. As discussed above, infiltration of picritic melt would induce partial melting of the troctolite mush. Melting of 20–30% troctolite (50–60 vol.% partial melt) mixed with 40–50 vol.% picrite results in REE concentrations in plagioclase similar to those measured in the anorthosite layer (Fig. S4). We suggest that the plagioclase zonation with calcic cores and more sodic and REE-enriched rims in the Unit 7–8 anorthosite (Figs. 5d and 12) developed with subsequent crystallisation from a more evolved (trapped) interstitial liquid. Further REE-based modelling (Fig. S4) suggests 40–70% fractional crystallisation of the proposed hybrid melt would be sufficient. Taken together, our data lend support to a replacive origin for the massive Unit 7–8 anorthosite layer, followed by postcumulus crystallisation of a relatively differentiated interstitial melt.

In addition to the anorthosite layer, autoliths of anorthositic composition are an important component of the upper portion of the Unit 7 troctolite. The presence of the anorthosite autoliths has been reported for other parts

of the ELI as well; e.g., the Unit 9 troctolite, typically in association with peridotite sills (Leuthold et al. 2014), and for the troctolite of Unit 14 (Renner and Palacz 1987; Volker and Upton 1990). However, little attention has previously been paid to the petrogenesis of the autoliths, despite their close association with the Cr-spinel seams. Importantly, the anorthosite autoliths described in this study also occur in areas without an overlying anorthosite layer (e.g., Localities 11) distal to the centre of the intrusion and some autoliths have rims of Cr-spinel (Fig. 2f). We argue that the similarities in mineral composition and texture, as well as their restricted occurrence in the upper 1–3 m of the Unit 7 troctolite, suggest a similar origin for the autoliths and the anorthosite layer, i.e. by dissolution and replacement of troctolite during a period of syn-magmatic deformation and melt infiltration. However, contrary to the main layer, assimilation occurred within the troctolite mush instead of at the level of new magma emplacement. If the anorthosite autoliths formed by partial dissolution of the troctolite, this would explain why they have such similar textural characteristics to the troctolite (i.e. the grain size distribution and aspect ratios of plagioclase crystals in each lithology). The peridotite schlieren are therefore interpreted as remnants of the downward-directed channelled flow infiltration process and thus likely represent the crystallisation product of this reacting agent in the assimilation process. Their ductile behaviour (Fig. 2e) supports the suggestion of syn-magmatic deformation, while the troctolite mush was at a high temperature. The flattened, ellipsoidal shapes and sharp boundaries of the autoliths indicate they were deformed with the host troctolite, and their locally developed sigmoidal shapes indicate solid-state deformation which might point to a rheological contrast between autolith and host during deformation. Indeed, such a contrast would be expected given the much lower ‘porosity’ of the anorthosite autoliths. The top-down-to-the-west shear sense supports the interpretation that deformation occurred during slumping of the ELI macro-rhythmic layers toward the LLF. The contrasting mineralogy of interstitial phases in the autoliths and the anorthosite layer also point to differences in their petrogenesis. The presence of interstitial clinopyroxene, hornblende and relatively REE-enriched rims all suggest the presence of more fractionated interstitial melts than those present in the anorthosite layer (where interstitial olivine is dominant). More speculatively, the irregularly-shaped anorthosite patches and autoliths with Cr-spinel seam rims probably represent a relatively late-stage of melt infiltration into the troctolite crystal mush.

### Chronology of the Unit 7–8 boundary formation

The combined observations on the field relations and petrography set out above provide insights into the timing of the respective stage(s) which formed the Unit 7–8 boundary

package. Most importantly, cross-cutting relations revealed by field observations as well as the new textural and geochemical data suggest that the Unit 7–8 boundary package was formed by multiple replenishment stages, or one major pulsed replenishment stage, instead of a single continuous magma influx. Our interpretation fits well with the ‘leaky’ open-system replenishment behaviour that has been attributed to other sections of the ELI (e.g., Brown 1956; Tait 1985). Interestingly, a multi-stage origin was also recently proposed for the well-known Merensky Reef of the Bushveld Complex (Chisyakova et al. 2019). In the latter study, the authors showed that the Merensky Reef was constructed in situ by several replenishment stages, indicating that precious metal ore deposit formation in layered intrusions in general may be a multi-stage process.

The cross-cutting relations in the central section of the Unit 7–8 boundary traverse are graphically summarised in Fig. 13. Notably, no lateral variations in cross-cutting relations were observed along strike, thus the general sequence of stages set out here is applicable for the Unit 7–8 boundary zone throughout the entire ELI. Peridotite schlieren and anorthosite autoliths are a ubiquitous feature along the complete traverse of the Unit 7 troctolite (Figs. 2e and 13), without any changes noted in their mode of occurrence, size or distribution. Moreover, deformation of the troctolite in the upper part of Unit 7 is observed throughout the studied traverse also. Given that the autoliths preserve evidence for a distinct intercumulus mineralogy, and have apparently been deformed as solid (or near solid) objects in the troctolite crystal mush, we suggest they were formed from a relatively early infiltration stage for which other evidence has been overprinted by subsequent infiltration (as represented by the peridotite schlieren and irregularly-shaped anorthosite patches). Cross-cutting of the peridotite schlieren and deformation structures in the troctolite by the overlying anorthosite layer (Figs. 2e and 13) indicates that the layer was formed at a later stage in the history of the crystal mush (i.e. after significant deformation had already affected the troctolite). The anorthosite layer, therefore, represents the product of a (possibly intrusion-wide) cumulate assimilation process, as previously described.

The formation of the anorthosite layer was followed by crystallisation of the Cr-spinel seam, which occasionally cross-cuts or pinches the underlying anorthosite (Figs. 3a and 13). In line with previous studies (cf. O’Driscoll et al. 2009b; 2010), we envisage in situ Cr-spinel seam crystallisation due to assimilation of the anorthosite layer by picritic melt. However, based on the indicative field observations of Cr-spinel seams cross-cutting the underlying anorthosite, we propose that the crystallisation stage occurred after the formation of the anorthosite layer, i.e. due to an additional (third) replenishment stage. Consequently, we propose that for the crystallisation of the Cr-spinel seam, anorthosite

instead of troctolite had to be assimilated. The proposed reaction can be illustrated in more detail using the forsterite-diopside-anorthite pseudo-ternary diagram (Fig. 13). The intruding parental magma of picritic composition ( $P$ , Upton et al. 2002,) assimilated anorthosite  $A$ , driving the hybrid melt  $S_1$  into the spinel stability field, crystallising (Cr-) spinel only at the expense of existing plagioclase and olivine. The observation that Cr-spinel crystals occur in corroded embayments in olivine (Fig. 5e) supports the proposed dissolution–crystallisation process. Our observation that the seams are typically cemented by plagioclase suggests that crystallisation followed a path to the An-L cotectic ( $S_2$ ), crystallising interstitial plagioclase until the peritectic point  $X$  was reached, where the liquid became oversaturated in silica resulting in the reaction where olivine and plagioclase crystallise at the expense of the (Cr-) spinel and melt. Following Rollinson (2008; see Table S4 for details of the algorithm used), the Cr-spinel parental melt  $Al_2O_3$  composition can be calculated to further constrain this assimilation process. The calculations result in concentrations of 16–17 wt.%  $Al_2O_3$  for the parental melt of Cr-spinel of the main seam. These values are best explained by a mixture of 80–90% of picrite (15.18 wt.%  $Al_2O_3$ ; Upton et al. 2002) and 10–20% anorthosite (~28 wt.%  $Al_2O_3$ ; O’Driscoll et al. 2009a). Thus, it is possible that relatively small amounts of anorthosite assimilation were sufficient to induce Cr-spinel crystallisation.

To crystallise the 1–2 mm thick seams, we argue for a dynamic setting, i.e. constant through flow of new picritic magma and assimilation of anorthosite without chemical equilibration of both agents. High degrees of melt–rock reaction are required to account for the Cr mass balance (i.e. the low concentration of Cr in the anorthosite and the picrite relative to the Cr-spinel seam; O’Driscoll et al. 2009b). The recognition that anorthosite might be the key assimilant for Cr-spinel seam formation could have important implications for the petrogenesis of Cr-spinel layers in other layered intrusions, like the UG1 layer of the Bushveld Complex. Indeed, Scoon and Costin (2018) showed that thin chromitite layers (so-called stringers) formed in the Upper Critical Zone of the Bushveld Complex due to assimilation of anorthosite by intruding picrite sills, resulting in markedly similar lithological associations and structures to those described here. Small circular depressions of the seam into the anorthosite (Fig. 2b) also indicate the thermal erosion caused by this magma sheet, similar to the potholes that ubiquitously occur in the footwall rocks to chromitite layers in the Bushveld Complex (cf. Latypov et al. 2017a), albeit over smaller length-scales in the ELI. Peridotite apophyses, oriented parallel to the foliation in the anorthosite layer and rimmed by subsidiary Cr-spinel seams (e.g., Localities 7, 12, 1; Figs. 3c and 4; Bédard et al. 1988) further highlight the close association of Cr-spinel seam formation and anorthosite. We

interpret these apophyses as thin melt channels of picritic melt that infiltrated the surrounding anorthosite and formed subsidiary Cr-spinel seams as ‘reaction rims’ completely surrounding the former melt channel (Fig. 5e). Similar reaction fronts, with Cr-spinel rims around clots of anorthosite were described by Bédard (1991, 1993) in the Bay of Islands Ophiolite, Newfoundland.

Subsequent crystallisation from the overlying picritic magma formed the basal part of the Unit 8 peridotite. Our study focuses on the boundary zone and thus only on the lowermost portion of the overlying Unit 8 peridotite; it has been shown that the latter itself was incrementally constructed, i.e. by multiple replenishment stages (Hepworth et al. 2020a), indicating that the leaky open-system behaviour continued after crystallisation of the Unit 7–8 Cr-spinel seam. The aforementioned findings of Hepworth et al. (2020a) imply that the original hanging wall contacts to the Unit 7–8 boundary zone magma replenishment stage were likely obliterated during subsequent construction of the Unit 8 peridotite.

The final step in the formation of the Unit 7–8 seam package was the complete solidification of the seam package, involving compositional modification and crystallisation of the interstitial melt. Cr-spinel is known to undergo postcumulus reequilibration (Roeder and Reynolds 1991; Kamenetsky et al. 2001; Barnes and Roeder 2001). In the ELI, chemical equilibration of Cr-spinel with the intercumulus melt resulted in an increase in  $Fe^{3+}$  and Ti content (Fe–Ti-trend; Lenaz et al. 2011; O’Driscoll et al. 2010). Our new compositional data (Fig. 8) suggest that Cr-spinel in the anorthosite layer reacted with the interstitial melt causing a marked increase in  $Fe^{3+}$  and Ti. The higher  $TiO_2$  concentrations of Cr-spinel observed in the anorthosite autoliths compared to those in the anorthosite layer suggest interaction with a more evolved interstitial liquid. Thus, we conclude that the Unit 7–8 boundary package was constructed over at least three separate stages. Footwall deformation overlapped with the early stages of magmatic emplacement, but was less significant in the later stages, suggesting a close interplay between the magma supply and deformation.

### Lateral variations of the Unit 7–8 boundary zone and implications for intrusive replenishment

In this study, the Unit 7–8 boundary zone was mapped and sampled along strike across the extent of the ELI, revealing lateral variations in its structure and geochemistry. Our observations are specifically placed in the context of an increasing number of studies that strongly suggest layered intrusions form by repeated intrusive emplacement of magma (e.g., Bédard et al. 1988; Mungall et al. 2016; Scoon and Costin 2018; Hepworth et al. 2017; 2018; 2020a; 2020b; Robb and Mungall 2020; Scoon et al.

2020), adding a new dimension to the complexity of Cr-spinel seam petrogenesis in these bodies.

Based on the spatially coupled occurrence of the anorthosite and Cr-spinel layer (Fig. 1) and the lateral changes in plagioclase and Cr-spinel mineral chemistry within the respective layers (Figs. 9 and 11), we suggest that the Unit 7–8 boundary package preserves the evidence of repeated intrusive magma replenishment. The intrusive replenishment model for Rum finds strong support in the work of Bédard et al. (1988), as well as recent studies by Hepworth et al. (2017; 2018, 2020a, 2020b). Lateral mineral chemical variations of the sort described here would likely not be preserved in the traditional open-system magma chamber model, whereas a more distinct thermal gradient between the replenishing magma and host rock (i.e. footwall cumulate) might be expected in an intrusive regime. Indeed, Hepworth et al. (2020b) recently demonstrated a rapid cooling history for repeated small volume intrusive magma inputs to the Rum system.

The replenishing magmas on Rum were likely to have been superheated with respect to olivine upon emplacement (Holness and Winpenny 2009; Upton et al. 2002). Prior work on the Rum harrisites (Donaldson 1974, 1979; O'Driscoll et al. 2007a) has shown that these rocks formed from aphyric picritic parental magmas that underwent relatively deep undercooling on emplacement. The observation that harrisites occur at the base of and throughout Unit 8 (Hepworth et al. 2020a), therefore, supports the suggestion that these magmas were present during the formation of the Unit 7–8 boundary package. In close proximity to the LLF, where these magmas first entered the intrusion, vigorous thermochemical erosion of the troctolite footwall would have been likely, preventing the formation of restitic anorthosite. We suggest that the highly deformed and brecciated intrusive zones in Unit 14 (southwest of Askival) and the CI of the Rum intrusion, as described in great detail by Volker and Upton (1990), might be the exposed penetration fronts of such intrusive sills. Moreover, subsequent slumping back towards the centre of the intrusion (Emeleus et al. 1996; O'Driscoll et al. 2007b) was likely more significant closer to the LLF, which would also account for the disturbed and stretched out units around Barkeval and the southeastern flank of Askival (e.g. McClurg 1982; Volker and Upton 1990; Hepworth et al. 2020a). In the central part of the ELI (Localities 7–10b), due to the cooling of the propagating sill, assimilation of the troctolite in the aforementioned process resulted in the formation of the anorthosite layer. With the maximum observed distance from the LLF, east of Hallival (Localities 11 and 17), the thermal capacity of the sill and potential to dissolve the troctolitic footwall were diminished, leading to the direct crystallisation of the Unit 8 peridotite on top of the Unit 7 troctolite.

Compositional changes in sills have frequently been described and interpreted to record temperature and fractionation trends (e.g., Jaupart and Tait 1995; Naslund 1989; Latypov 2003). Naslund (1989) reported variations in mineral chemistry of olivine, pyroxene and plagioclase in the Basistoppen Sill, East Greenland, suggesting fractionation across the extent of the ~600 m thick sill, while Latypov (2003) proposed that similar trends would develop in magmas injected into consolidating igneous rocks. We argue that the lateral chemical variations observed here are permissive of the type of thermal regime that might be developed in a sill-like intrusion. In particular, the compositional changes in plagioclase in the anorthosite layer and Cr-spinel in the seam with distance from the LLF may reflect a temperature reduction in the magma with increasing distance from its feeder zone (Fig. 11), thus following the experimental trends described by Leuthold et al. (2015; Fig. 8). Furthermore, the co-variation of plagioclase and Cr-spinel along the traverse argues for an inherited primary magmatic signal instead of a postcumulus equilibration artefact. Moreover, localised metasomatism, recently described for the Unit 8 peridotite (Hepworth et al. 2020a), could obscure the described lateral trends further and possibly accounts for the differing petrography and mineral chemistry of Locality 13. There is additional complexity, however, in that multiple episodes of magma intrusion are implied by the combined observations here, and each has the effect of partially overprinting the effects of the last. That each of these replenishments occurred along the same approximate footwall plane within the intrusion may have been a consequence of a structural control, given the observed close association of deformation and magmatism.

## Conclusions

We investigated the Unit 7–8 Cr-spinel seam and associated hanging wall and footwall lithologies over the lateral extent of the ELI by carrying out field documentation as well as microstructural and mineral chemistry analyses, revealing significant lateral variations in the macro-to-microstructural and mineral chemical character of the package of rocks. Our observations elucidate the timing and interplay of magmatic influxes and deformation of the crystal pile in the Rum intrusion, which finally resulted in the formation of the Cr-spinel seam and the Unit 7–8 boundary package more generally. We find that the Cr-spinel seam and associated rocks were constructed by multiple replenishment stages, possibly linked to variations in magma flux and ambient syn-magmatic deformation. Importantly, we demonstrate that the nature and extent of the replenishing stages and thus the interactions with the underlying cumulates (e.g., assimilation, Cr-spinel

crystallisation) varied along strike within the intrusion. Our study highlights the close connection of anorthosite and PGE-bearing Cr-spinel seams and suggests that, on Rum, proximity to the magma feeder zone and the availability of primitive reactive parental melt was essential for Cr-spinel seam formation. In general, our findings may help to constrain the formation of precious metal enriched Cr-spinel seams in other layered intrusion such as the Merensky Reef of the Bushveld Complex. The seams from both intrusions are very similar in character insofar as they formed in multi-stage events and they share a coupled anorthosite-Cr-spinel seam association. Thus, a fruitful avenue for future research would be to test the hypothesis that anorthosite assimilation was a critical step for Cr-spinel seam formation in the Bushveld Complex.

**Acknowledgements** Open Access funding provided by Projekt DEAL. FEDK was supported by the German Federal Ministry of Education and Research (BMBF), grant FKZ 033R119C. Sampling permission on Rum from Scottish National Heritage (SNH) in 2016 is highly appreciated. We are grateful to M. Oeser-Rabe and S. Schuth for their support with the LA-ICP-MS analyses at the Leibniz University of Hannover and to K. Born and P. Czaja for their support at the SEM and electron microprobe at the Museum für Naturkunde Berlin. We are very grateful to Jean H Bédard and an anonymous reviewer for their detailed and helpful comments, as well as to Othmar Müntener for thoughtful editorial handling.

**Open Access** This article is licensed under a Creative Commons Attribution 4.0 International License, which permits use, sharing, adaptation, distribution and reproduction in any medium or format, as long as you give appropriate credit to the original author(s) and the source, provide a link to the Creative Commons licence, and indicate if changes were made. The images or other third party material in this article are included in the article's Creative Commons licence, unless indicated otherwise in a credit line to the material. If material is not included in the article's Creative Commons licence and your intended use is not permitted by statutory regulation or exceeds the permitted use, you will need to obtain permission directly from the copyright holder. To view a copy of this licence, visit <http://creativecommons.org/licenses/by/4.0/>.

## References

- Ashwal LD (1993) Anorthosites. Springer, Berlin, Heidelberg
- Barnes SJ, Roeder PL (2001) The range of spinel compositions in terrestrial mafic and ultramafic rocks. *J Petrol* 42:2279–2302
- Bédard JH (1991) Cumulate recycling and crustal evolution in the bay of islands ophiolite. *J Geol* 99:225–249
- Bédard JH (1993) Oceanic crust as a reactive filter: synkinematic intrusion, hybridization, and assimilation in an ophiolitic magma chamber, western Newfoundland. *Geology* 11:77–80
- Bédard JH, Sparks RSJ, Renner R, Cheadle MC, Hallworth MA (1988) Peridotite sills and metasomatic gabbros in the eastern layered series of the Rhum complex. *J Geol Soc* 145:207–224
- Boorman S, Boudreau AE, Kruger FJ (2004) The lower zone-critical zone transition of the bushveld complex: a quantitative textural study. *J Petrol* 45:1209–1235
- Brown GM (1956) The layered ultrabasic rocks of Rhum, inner hebrides. *Philos Trans R Soc London Ser B* 240:1–54
- Butcher AR, Pirrie D, Prichard HM, Fisher P (1999) Platinum-group mineralization in the rum layered intrusion, Scottish Hebrides, UK. *J Geol Soc* 156:213–216
- Chisyakova S, Latypov R, Youlton K (2019) Multiple merensky reef of the Bushveld complex, South Africa. *Contrib Miner Petrol* 174:1–17
- Donaldson CH (1974) Olivine crystal types in harrisitic rocks of the Rhum pluton and in Archean spinifex rocks. *Geol Soc Am Bull* 85:1721–1726
- Donaldson CH (1979) An experimental investigation of the delay in nucleation of olivine in mafic magmas. *Contrib Miner Petrol* 69:21–32
- Donaldson CH (1985) The rates of dissolution of olivine, plagioclase, and quartz in a basalt melt. *Miner Mag* 49:683–693
- Droop GTR (1987) A general equation for estimating Fe<sup>3+</sup> concentrations in ferromagnesian silicates and oxides from microprobe analyses, using stoichiometric criteria. *Miner Mag* 51:431–435
- Dunham AC, Wadsworth WJ (1978) Cryptic variation in the Rhum layered intrusion. *Miner Mag* 42:347–356
- Dunham AC, Wilkinson FCF (1985) Sulphide droplets and the Unit 11/12 chromite band, Rhum: a mineralogical study. *Geol Mag* 122:539–548
- Emeleus CH (1994) 1: 20000 solid geology map of Rum. Scottish Natural Heritage, Inverness
- Emeleus CH (1997) Geology of Rum and the adjacent islands. Memoir of the British Geological Survey, Sheet 60 (Scotland)
- Emeleus CH, Cheadle MC, Hunter RH, Upton BGJ, Wadsworth WJ (1996) The Rum layered suite. In: Cawthorn RG (ed) Layered intrusions. Elsevier, Amsterdam, pp 403–439
- Guillong M, Meier D, Allan MM, Heinrich CA, Yardley BWD (2008) SILLS: a MATLAB-based program for the reduction of laser ablation ICP-MS data of homogeneous materials and inclusions. *Miner Assoc Can Short Course* 40:328–333
- Hamilton MA, Pearson DG, Thompson RN, Kelley SP, Emeleus CH (1998) Rapid eruption of Skye lavas inferred from precise U-Pb and Ar-Ar dating of the Rum and Cuillin plutonic complexes. *Nature* 394:260–263
- Harker A (1908) The Geology of the Small Isles of Invernessshire. Memoir of the Geological Survey: Scotland, Edinburgh
- Henderson P (1975) Reaction trends shown by chrome-spinels of the Rhum layered intrusion. *Geochim Cosmochim Acta* 39:1035–1044
- Henderson P, Suddaby P (1971) The nature and origin of the chrome-spinel of the Rhum layered intrusion. *Contrib Miner Petrol* 33:21–31
- Hepworth LN, O'Driscoll B, Gertisser R, Daly JS, Emeleus CH (2017) Incremental construction of the unit 10 Peridotite, Rum eastern layered intrusion, NW Scotland. *J Petrol* 58:137–166
- Hepworth LN, O'Driscoll B, Gertisser R, Daly JS, Emeleus CH (2018) Linking in situ crystallization and magma replenishment via sill intrusion in the Rum western layered intrusion, NW Scotland. *J Petrol* 59:1605–1642
- Hepworth LN, Kaufmann FED, Hecht L, Gertisser R, O'Driscoll B (2020a) Braided peridotite sills and metasomatism in the Rum layered suite, Scotland. *Contrib Miner Petrol* 175:1–25
- Hepworth LN, Daly JS, Gertisser R, Johnson CG, Emeleus CH, O'Driscoll B (2020b) Rapid crystallization of precious-metal-mineralized layers in mafic magmatic systems. *Nat Geosci* 13:375–381
- Higgins MD (2000) Measurement of crystal size distributions. *Am Mineral* 85:1105–1116
- Holness MB (1999) Contact metamorphism and anatexis of torridonian arkose by minor intrusions of the Rum igneous complex, inner hebrides, Scotland. *Geol Mag* 135:527–542

- Holness MB (2014) The effect of crystallization time on plagioclase grain shape in dolerites. *Contrib Miner Petrol* 168:1–19
- Holness MB, Wimpenny B (2009) The unit 12 allivalite, eastern layered intrusion, Isle of Rum: a textural and geochemical study of an open-system magma chamber. *Geol Mag* 146:437–450
- Holness MB, Neufeld JA, Gilbert AJ, Macdonald R (2017) Orientation of tabular mafic intrusions controls convective vigour and crystallization style. *J Petrol* 58:2035–2053
- Irvine TN (1975) Crystallization sequences in the Muskox intrusion and other layered intrusions-II. Origin of chromitite layers and similar deposits of other magmatic ores. *Geochim Cosmochim Acta* 33:991–1020
- Irvine TN (1977) Origin of chromitite layers in the Muskox intrusion and other stratiform intrusions: a new interpretation. *Geology* 5:273–277
- Jarosewich E, Nelen JA, Norberg JA (1980) Reference samples for electron microprobe analysis. *Geostand Geoanal Res* 4:43–47
- Jaupart C, Tait S (1995) Dynamics of differentiation in magma reservoirs. *J Geophys Res Solid Earth* 100:17615–17636
- Kamenetsky VS, Crawford AJ, Meffre S (2001) Factors controlling chemistry of magmatic spinel: an empirical study of associated olivine, Cr-spinel and melt inclusions from primitive rocks. *J Petrol* 42:655–671
- Latypov R (2003) The origin of basic-ultrabasic sills with S-, D-, and I-shaped compositional profiles by in situ crystallization of a single input of phenocryst-poor parental magma. *J Petrol* 44:1619–1656
- Latypov R, O'Driscoll B, Lavrenchuk A (2013) Towards a model for the in situ origin of PGE reefs in layered intrusions: insights from chromitite seams of the Rum eastern layered intrusion, Scotland. *Contrib Miner Petrol* 166:309–327
- Latypov R, Chisyakova S, Page A, Hornsey R (2015) Field evidence for the in situ crystallization of the merensky reef. *J Petrol* 56:2341–2372
- Latypov R, Chisyakova S, Mukherjee R (2017a) A novel hypothesis for origin of massive chromitites in the Bushveld igneous complex. *J Petrol* 58:1899–1940
- Latypov R, Chisyakova S, Barnes SJ, Hunt EJ (2017b) Origin of platinum deposits in layered intrusions by in situ crystallization: evidence from undercutting merensky reef of the Bushveld complex. *J Petrol* 58:715–761
- Latypov R, Chisyakova S, Costin G, Namur O, Barnes S, Kruger W (2020) Monomineralic anorthosites in layered intrusions are indicators of the magma chamber replenishment by plagioclase-only-saturated melts. *Sci Rep* 10:1–14
- Lazarov M, Horn I (2015) Matrix and energy effects during in-situ determination of Cu isotope ratios by ultraviolet-femtosecond laser ablation multicollector inductively coupled plasma mass spectrometry. *Spectrochim Acta Part B At Spectrosc* 111:64–73
- Lenaz D, O'Driscoll B, Princiville F (2011) Petrogenesis of the anorthosite-chromitite association: crystal-chemical and petrological insights from the Rum layered suite, NW Scotland 162:1201–1213
- Leuthold J, Blundy JD, Holness MB, Sides R (2014) Successive episodes of reactive liquid flow through a layered intrusion (unit 9, Rum eastern layered intrusion, Scotland). *Contrib Miner Petrol* 168:1–27
- Leuthold J, Blundy JD, Brooker RA (2015) Experimental petrology constraints on the recycling of mafic cumulate: a focus on Cr-spinel from the Rum eastern layered intrusion. *Scotland* 170:1–12
- McClurg (1982) Petrology and Evolution of the Northern Part of the Rhum Ultrabasic Complex. Unpublished Ph.D. Thesis, University of Edinburgh
- Meurer WP, Boudreau AE (1998) Compaction of igneous cumulates part ii: compaction and the development of igneous foliations. *J Geol* 106:293–304
- Morse SA (1980) Basalts and phase diagrams: an introduction to the quantitative use of phase diagrams in igneous petrology. Springer, New York
- Mungall JE, Kamo SA, McQuade S (2016) U-Pb geochronology documents out-of-sequence emplacement of ultramafic layers in the Bushveld Igneous Complex of South Africa. *Nat Commun* 7:1–13
- Namur O, Abily B, Boudreau AE, Blanchette F, Bush JWM, Ceuleneer G, Charlier B, Donaldson CH, Duchesne JC, Higgins MD, Morata D, Nielsen TFD, O'Driscoll B, Pang KN, Peacock T, Spandler C, Toramaru A, Veksler IV (2015) Igneous layering in basaltic magma chambers. In: Charlier B, Namur O, Latypov R, Tegner C (eds) Layered intrusions. Springer, Dordrecht, pp 75–152
- Naslund HR (1989) Petrology of the basistoppen sill, east Greenland: a calculated magma differentiation trend. *J Petrol* 30:299–319
- O'Driscoll B, Donaldson CH, Troll VR, Jerram DA, Emeleus CH (2007a) An origin for harrisitic and granular olivine in the Rum layered suite, NW Scotland: a crystal size distribution study. *J Petrol* 48:253–270
- O'Driscoll B, Hargraves RB, Emeleus CH, Troll VR, Donaldson CH, Reavy RJ (2007b) Magmatic lineations inferred from anisotropy of magnetic susceptibility fabrics in Units 8, 9, and 10 of the Rum eastern layered series, NW Scotland. *Lithos* 98:27–44
- O'Driscoll B, Day JMD, Daly JS, Walker RJ, McDonough WF (2009a) Rhenium-osmium isotopes and platinum-group elements in the Rum layered Suite, Scotland: Implications for Cr-spinel seam formation and the composition of the Iceland mantle anomaly. *Earth Planet Sci Lett* 286:41–51
- O'Driscoll B, Donaldson CH, Daly JS, Emeleus CH (2009b) The roles of melt infiltration and cumulate assimilation in the formation of anorthosite and a Cr-spinel seam in the Rum eastern layered intrusion, NW Scotland. *Lithos* 111:6–20
- O'Driscoll B, Emeleus CH, Donaldson CH, Daly JS (2010) Cr-spinel seam petrogenesis in the Rum layered suite, NW Scotland: cumulate assimilation and in situ crystallization in a deforming crystal mush. *J Petrol* 51:1171–1201
- Oeser M, Weyer S, Horn I, Schuth S (2014) High-precision Fe and Mg isotope ratios of silicate reference. *Geostand Geoanal Res* 38:311–328
- Power MR, Pirrie D, Andersen JØ, Wheeler PD (2000) Testing the validity of chrome spinel chemistry as a provenance and petrogenetic indicator. *Geology* 28:1027–1030
- Power MR, Pirrie D, Andersen JØ (2003) Diversity of platinum-group element mineralization styles in the north atlantic igneous province: new evidence from Rum, UK. *Geol Mag* 140:499–512
- Renner R, Palacz Z (1987) Basaltic replenishment of the Rhum magma chamber: evidence from unit 14. *J Geol Soc* 144:961–970
- Robb SJ, Mungall JE (2020) Testing emplacement models for the rustenburg layered suite of the bushveld complex with numerical heat flow models and plagioclase geospeedometry. *Earth Planet Sci* 534:1–12
- Roeder RL, Reynolds I (1991) Crystallization of chromite and chromium solubility in basaltic melts. *J Petrol* 32(5):909–934
- Rollinson H (2008) The geochemistry of mantle chromitites from the northern part of the Oman ophiolite: inferred parental melt composition. *Contrib Miner Petrol* 156:273–288
- Scoon RN, Costin G (2018) Chemistry, morphology and origin of magmatic-reaction chromite stringers associated with anorthosite in the upper critical zone at Winnaarshoek, eastern limb of the bushveld complex. *J Petrol* 59:1551–1578
- Scoon RN, Costin G, Mitchell A, Moine B (2020) Non-sequential injection of PGE-rich ultramafic sills in the platereef unit at Akanani, northern limb of the bushveld complex: evidence from Sr and Nd isotopic systematics. *J Petrol*. <https://doi.org/10.1093/petrology/egaa032>
- Sun C, Graff M, Liang Y (2017) Trace element partitioning between plagioclase and silicate melt: the importance of temperature and plagioclase composition, with implications for terrestrial and lunar magmatism. *Geochim Cosmochim Acta* 206:273–295
- Tait SR (1985) Fluid dynamic and geochemical evolution of cyclic unit 10, Rhum, eastern layered series. *Geol Mag* 122:469–484

- Upton BGJ, Skovgaard AC, McClurg J, Kirstein L, Cheadle MC, Emeleus CH, Wadsworth WJ, Fallick AE (2002) Picritic magmas and the Rum ultramafic complex, Scotland. *Geol Mag* 139:437–452
- Volker JA, Upton BGJ (1990) The structure and petrogenesis of the trall-val and ruinsival areas of the Rhum ultrabasic complex. *Trans R Soc Edinb, Earth Sci* 81:69–88
- Wager LR, Brown GM (1967) Wager, Lawrence Rickard, and George Malcolm Brown. Layered igneous rocks. WH Freeman, Edinburgh
- Wall CJ, Scoates JS, Weis D, Friedman RM, Amini M, Meurer WP (2018) The stillwater complex: integrating zircon geochronological and geochemical constraints on the age, emplacement history and crystallization of a large, open-system layered intrusion. *J Petrol* 59:153–190
- Young IM (1984) Mixing of supernatant and interstitial fluids in the Rhum layered intrusion. *Miner Mag* 48:345–350

**Publisher's Note** Springer Nature remains neutral with regard to jurisdictional claims in published maps and institutional affiliations.